Predicting mixing via resonances: Application to spherical piecewise isometries

Lachlan D. Smith,[1,*] Paul P. Park,[2] Paul B. Umbanhowar,[3] Julio M. Ottino,[1,3,4] and Richard M. Lueptow[3,4,†]
[1]*Department of Chemical and Biological Engineering, Northwestern University, Evanston, Illinois 60208, USA*
[2]*Department of Engineering Sciences and Applied Mathematics, Northwestern University, Evanston, Illinois 60208, USA*
[3]*Department of Mechanical Engineering, Northwestern University, Evanston, Illinois 60208, USA*
[4]*The Northwestern Institute on Complex Systems (NICO), Northwestern University, Evanston, Illinois 60208, USA*
(Received 3 March 2017; published 13 June 2017)

We present an analytic method to find the areas of nonmixing regions in orientation-preserving spherical piecewise isometries (PWIs), and apply it to determine the mixing efficacy of a class of spherical PWIs derived from granular flow in a biaxial tumbler. We show that mixing efficacy has a complex distribution across the protocol space, with local minima in mixing efficacy, termed resonances, that can be determined analytically. These resonances are caused by the interaction of two mode-locking-like phenomena.

DOI: 10.1103/PhysRevE.95.062210

I. INTRODUCTION

Mixing is central to a wide range of industries. While fluid mixing by "stretching and folding" in time-periodic flows has been studied extensively and is relatively well understood [1–3], mixing of granular materials has received less attention. Granular materials are pervasive, spanning, for example, the pharmaceutical and food processing industries where achieving homogeneous mixtures of granular ingredients is critical. However, most studies on granular mixing consider two-dimensional (2D) flows, and those that consider three-dimensional (3D) granular mixing primarily consider the effectiveness of industrial mixing devices rather than the underlying mechanics and mathematics of the fundamental mixing processes [4–6].

In practice, mixing in granular flows can result from collision driven diffusion, chaotic advection (stretching and folding), and spatial rearrangement of entire sections of material ("cutting and shuffling") [7] depending on the geometry and driving of the flow. The combination of and competition between these mechanisms results in complex motion of individual particles and significant challenges in understanding and predicting the overall mixing efficacy. For a class of mixing protocols in a spherical tumbler, isolating the cutting-and-shuffling motions yields a "skeleton" for the kinematics that captures the most significant mixing features observed in the corresponding experiments [8]. These cutting-and-shuffling transformations are termed *piecewise isometries* (PWIs) [9–11], which have found use in several applications [12–17]. In a PWI, an object is cut into several pieces, and the pieces are rearranged to reconstruct the original object. The theory of PWIs provides a framework to study the cutting-and-shuffling motions that drive granular mixing. However, this theory is still under development, and much remains to be understood. For instance, much of the theory has been developed for PWIs in planar geometry, and less is understood for PWIs in curved geometries such as a sphere [14,15,18,19], which is considered here. For planar PWIs generated by a single rotation angle θ the general nature of particle motion can be predicted based on whether θ/π is rational or irrational [13]. When θ/π is rational, the nonmixing regions form a polygonal tiling of the domain, and the mixing region has zero area. In contrast, when θ/π is irrational, the nonmixing regions are circular, and the mixing region has positive area.

For spherical PWIs generated by rotation like those considered here, similar predictions cannot be made because the composition of rotations in 3D is not as simple as summing the angles. Another feature of spherical PWIs is that translations are also rotations, meaning spherical PWIs consist of only rotations and reflections. Therefore, all spherical PWIs can be written piecewise as the composition of rotations and reflections. If no reflections occur, i.e., the PWI consists purely of rotation transformations, then the PWI is described as orientation preserving; otherwise, it is orientation reversing. Here, orientation-preserving PWIs are primarily considered, though the results are generic to orientation-reversing PWIs as well.

Linking the inherent geometric properties of PWIs with their mixing efficacy, Park *et al.* [18,19] demonstrated positive correlation between the area of the exceptional set (where the cuts occur) and the long-term mixing efficacy a spherical PWI produces. Essentially, portions of the domain covered by the exceptional set are eventually cut into arbitrarily small pieces that are rearranged, resulting in mixing. Therefore, if a large portion of the domain is covered by the exceptional set, then the mixing efficacy is high. Regions that are not covered by the exceptional set, called *cells* in PWI theory, remain intact for all time, and prevent mixing. These cells are analogous to nonmixing "islands" associated with elliptic periodic points of area-preserving dynamical systems. For mixing applications, it is desired to find protocols that maximize the area of the exceptional set and avoid protocols that minimize this area. We use the term *resonance* to denote a local minimum of exceptional set area in the protocol space because the total area occupied by cells is large, and so a large portion of the domain is periodic, i.e., resonating with itself. One method to find resonances is to compute the area of the exceptional set across the entire protocol space, which is computationally expensive. The question we address here is whether resonances, and hence mixing efficacy, can be predicted *a priori* based only on properties such as symmetry and limiting behavior of the PWI. By finding the areas of cells

*lachlan.smith@northwestern.edu
†r-lueptow@northwestern.edu

analytically, we identify resonances in the two-dimensional protocol space of an orientation-preserving spherical PWI. In doing so, we rationalize the complex distribution of mixing efficacy across the protocol space that was found by Juarez *et al.* [20].

We begin by introducing the biaxial spherical tumbler (BST) PWI and the relevant terminology from PWI theory in Sec. II A. Then, the complex distribution of mixing efficacy across the protocol is discussed and resonances demonstrated in Sec. II B. Finally, in Sec. III a method to find these resonances analytically is introduced and used to determine mixing efficacy across the protocol space.

II. RESONANCES IN A HEMISPHERICAL PWI

A. Biaxial spherical tumbler PWI

Here, we consider the half-full biaxial spherical tumbler (BST) PWI [7,18,20–22], which maps the hemispherical shell (HS) $S = \{(x,y,z) : x^2 + y^2 + z^2 = 1, y \leqslant 0\}$ to itself [23]. The map $M_{\theta_z,\theta_x} : S \to S$ originates from the vanishing flowing layer limit of a granular flow in a half-full spherical tumbler [7] and is given by the following sequence of transformations, referring to Fig. 1 and Park *et al.* [18]:

(1) Rotate the entire HS clockwise about the z axis by θ_z and make a cut through the HS in the $y = 0$ plane.

(2) Rotate the cut portion above $y = 0$ by π about the z axis to recover the HS.

(3) Repeat step 1, except perform the rotation anticlockwise about the x axis by θ_x.

(4) Repeat step 2, except perform the rotation about the x axis.

Here, θ_z,θ_x are the control parameters, and the ordered pair (θ_z,θ_x) is referred to as a protocol.

While the four-step description of the map uses two separate rotations and cuts, corresponding to the action of experimental granular tumblers [8], the map is identical to a single cut and shuffle transformation: cut the HS into four partial lunes P_{1-4}, termed *atoms* in PWI theory, as shown in Fig. 2(a), and rearrange them as shown in Fig. 2(b) to reconstruct the HS. Note that the atoms are labeled from right to left and top to bottom to reflect the general direction of tracer particle transport; particles move from right to left under the z-axis rotation, then from top to bottom under the x-axis rotation. We call the three curves $\mathcal{D}_{1-3}$ that separate the atoms "cutting lines," together they form the set $\mathcal{D} = \bigcup_{i=1}^{3} \mathcal{D}_i = \bigcup_{i,j,i\neq j}(P_i \cap P_j)$. For the BST PWI, $\mathcal{D}_{1-3}$ are generated as rotations of the domain boundary $\partial S : x^2 + z^2 = 1$, $y = 0$ about the x and z axes, and hence are sections of great circles, i.e., intersections of the sphere with a plane that passes through the origin. Tracking $\mathcal{D}$ forward and backward in time reveals all possible cut locations. For example, the cutting lines $\mathcal{D}$ separate regions that are cut and shuffled after one iteration, as demonstrated in Fig. 2. Combining $\mathcal{D}$ with its first preimage, $M^{-1}_{\theta_z,\theta_x}(\mathcal{D}) \cup \mathcal{D}$, separates regions that are cut and shuffled after two iterations, and so on. The entire set of images and preimages,

$$E = \bigcup_{n=-\infty}^{+\infty} M^n_{\theta_z,\theta_x}(\mathcal{D}), \tag{1}$$

is known as the *exceptional set* associated with the protocol (θ_z,θ_x). Due to the infinite union, it is impossible, in most cases, to find every point in the exceptional set. We numerically approximate E by seeding points along the cutting lines $\mathcal{D}$ and iterating them under the inverse map $M^{-1}_{\theta_z,\theta_x}$ to approximate each preimage. Combining a sufficient number of preimages [24] results in an approximation of E, examples of which are shown in Fig. 3 for different protocols (θ_z,θ_x).

Even though E always has zero Lebesgue measure (i.e., area), as it is the countable union of measure-zero sets, Park *et al.* have demonstrated that the closure $\bar{E} = E \cup \partial E$ is a "fat fractal" for most protocols [19], meaning it has positive Lebesgue measure and a fractal boundary. Furthermore, the area that $\bar{E}$ occupies correlates strongly with the long-term mixing achieved by the BST PWI [19], and this is expected to be a generic property of all PWIs. In essence, any region covered by $\bar{E}$ will eventually be cut into infinitely small pieces and rearranged, producing a high degree of mixing. While theoretically possible, the exceptional set generally does not cover the entire HS, but rather has "holes" termed *cells*, which are demonstrated by the white and colored regions in Fig. 3. Like nonmixing islands associated with elliptic periodic points in dynamical systems, these cells correspond to regions that are periodic, i.e., they return to their initial position after some number of iterations. The order in which each cell visits the atoms P_{1-4} before returning to its original position defines a unique periodic *itinerary*, e.g., in Fig. 3 the dark red cell in P_4 has itinerary $P_4 \to P_1 \to P_1$, or $411 = 41^2$ in short. Due to this uniqueness, each cell can be identified by its periodic itinerary. Note, however, that there may exist itineraries that do not correspond to a cell. A cell's periodic itinerary determines the sequence of isometries that a tracer particle inside the cell experiences. For instance, in P_4 particles are rotated by $\theta_z + \pi$

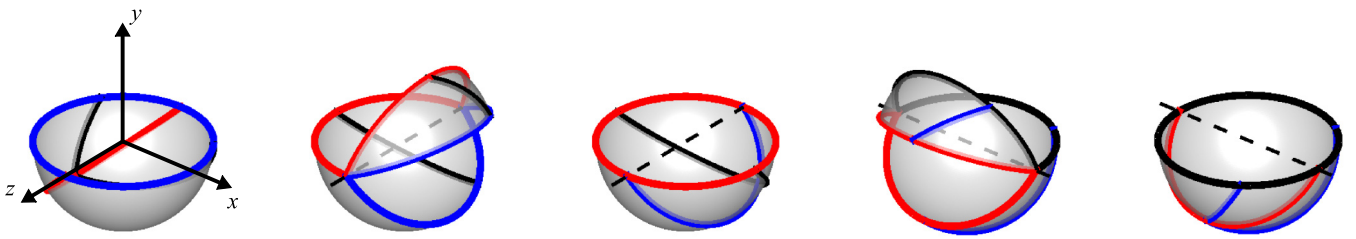

(a) Initial condition (b) Rotation and cut: z axis (c) After step 2 (d) Rotation and cut: x axis (e) After step 4

FIG. 1. The BST PWI for $\theta_z = \theta_x = \pi/4$. The solid blue, black, and red curves show where cutting occurs, and the dashed lines show the rotation axes. Adapted with permission from Park *et al.* [18] (©2016 AIP Publishing).

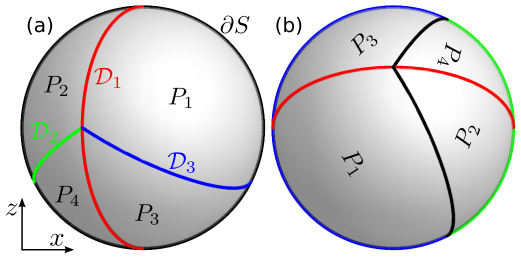

FIG. 2. Bottom view of the action of the BST PWI. The HS is cut along the curves $\mathcal{D}_{1-3}$ shown in (a) and recombined as shown in (b).

about the z axis, denoted $R^z_{\theta_z+\pi}$, then by $\theta_x+\pi$ about the x axis, denoted $R^x_{\theta_x+\pi}$, whereas in P_1 particles are rotated by $R^z_{\theta_z}$ then $R^x_{\theta_x}$. Therefore, all particles in the cell with itinerary 41^2 experience the same sequence of isometries:

$$\left(R^x_{\theta_x}R^z_{\theta_z}\right)\left(R^x_{\theta_x}R^z_{\theta_z}\right)\left(R^x_{\theta_x+\pi}R^z_{\theta_z+\pi}\right), \tag{2}$$

which will have important consequences in Sec. III where cell locations and sizes are found from the sequence of isometries associated with their itineraries.

By definition cells are periodic regions, and the iterates of a cell are also cells, with itineraries given by the rotation permutations of the original itinerary, e.g., the dark red cells in Figs. 3(a)–3(c) have itineraries 411, 141, and 114 and are iterates of each other. Therefore, we can refer to the entire set of iterates of a cell by specifying a single "base itinerary." Since all cells with the same base itinerary are solid body transformations of the base cell, they all have the same radius and share the same internal rotation angle α, i.e., the angle of rotation produced within the cell after it returns to its initial position, demonstrated by the white square in Fig. 3(b) that is rotated by $\alpha = 4\pi/5$ about the center of the cell after three iterations.

Furthermore, each chain of cells with a cell in P_4 is conjugate to another chain with the same period and size (Appendix B). This relationship is demonstrated by the two period-3 cell chains (dark red and light blue) in Figs. 3(a)–3(c) and the two period-6 cell chains (dark blue and light red) in Fig. 3(c). This conjugacy means that the characteristic information (radius, area, internal rotation angle) for one chain of cells is identical to that for a conjugate chain of cells.

Cells can manifest either as circles, regular polygons, or irregular polygons. The shape of the cell is determined by the rotation α produced within the cell after it returns to its initial position as follows [13,14]:

(i) Circles: internal rotation is incommensurate with π, i.e., α/π is irrational. These are demonstrated by the dark red, light blue, and white cells in Fig. 3(a). While the cells as a whole return to their initial location, they never return to their initial orientation, i.e., points inside the cells (other than the center) never return to their initial position.

(ii) Regular polygons: internal rotation is commensurate with π, i.e., $\alpha/\pi = 2p/q$ for some integers $p,q \neq 0$. In this case, the cell is a regular q-gon, for example, the dark red and light blue pentagons in Fig. 3(b) have $\alpha/\pi = 4/5$. Since each pentagon is period-3, after $3q = 15$ iterations they will return to their initial location with their initial orientation.

(iii) Irregular polygons: internal rotation $\alpha = 0$. These are demonstrated by the orange quadrilaterals and white triangles in Fig. 3(b). These irregular polygons do not rotate when they return to their initial positions.

Resonances occur when the combined size of all the cells is a local maximum in the protocol space or, equivalently, when the area of $\bar{E}$ is a local minimum. Therefore, resonances correspond to local minima in mixing efficacy. An extreme case occurs when the entire domain is periodic and the cells form a polygonal tiling of the HS. In this case no mixing occurs, as the domain periodically reassembles itself. For instance, in Fig. 3(b) the HS is tiled by regular pentagons (dark red and light blue), irregular quadrilaterals (orange), and irregular triangles (white). While polygonal tilings and fractal polygonal tilings are common in planar PWIs [11,13,14] due to the fact that composition of rotations is equivalent to the summation of angles, and isolated polygonal cells are relatively easy to find in spherical PWIs [14], we are not aware of any previous observations of polygonal tilings for PWIs in curvilinear geometries. We show in Sec. III B that the BST PWI produces an infinite family of polygonal tilings.

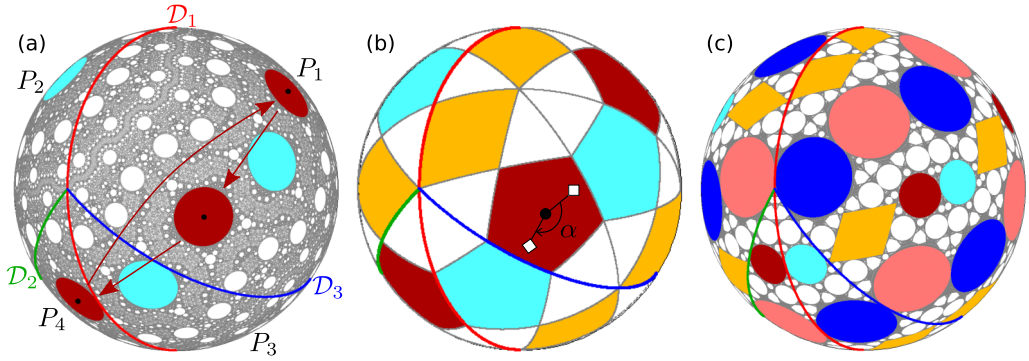

FIG. 3. Exceptional sets (gray) for the BST PWI with the cutting lines $\mathcal{D}_{1-3}$ shown red, green, and blue, respectively. Cells with base periodic itinerary $P_4 \to P_1 \to P_1$ ($411 = 41^2$) are shown in dark red, and the conjugate pair with base periodic itinerary $P_3 \to P_2 \to P_1$ (321) is shown in light blue. (a) For $\theta_z = \theta_x = 4\pi/15$ cells are circular and $\bar{E}$ has positive area. (b) For $\theta_z = \theta_x = \arccos[(-1+\sqrt{5})/2]$ the union of the regular pentagonal cells (dark red, light blue), the irregular quadrilateral cells (orange with itinerary 2131^2), and the irregular triangular cells (white with itineraries $31^241^221^3$ and 32131^421) perfectly tile the HS, which means $\bar{E}$ has zero area. (c) For $(\theta_z,\theta_x) = (0.9960,0.5748)$, both circular and polygonal cells exist, and $\bar{E}$ has finite area. Irregular quadrilateral cells are shown orange, cells with base itinerary 41^221^2 are shown light red, and their conjugate with base itinerary 321^221 is shown in dark blue.

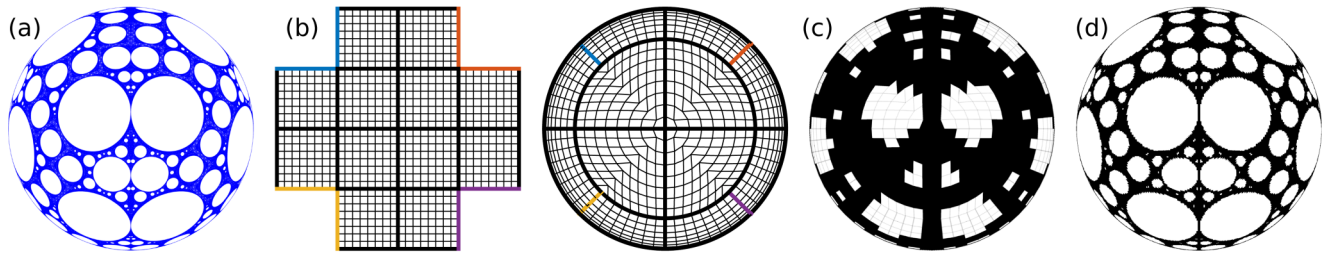

FIG. 4. Characterization of the area of the exceptional set by domain discretization. (a) The exceptional set for $(\theta_z,\theta_x) = (\pi/2,\pi/4)$. (b) Unfolded isocube half and isocube half mapped onto the HS, with $N = 12 \times 2^3 \times 2^3$ boxes. (c) Isocube half with grid shown in gray and boxes containing a point in the exceptional set colored black. (d) The same as (c) except $N = 12 \times 2^6 \times 2^6$ boxes are used, the isocube grid is not shown. (Adapted with permission from Park *et al.* [19], ©2017 American Physical Society.)

B. Mixing across the protocol space

Using the method described by Park *et al.* [19] to characterize mixing based on coverage of the exceptional set $\bar{E}$, the fraction of the HS covered by $\bar{E}$ is approximated by dividing the HS into $N = 12 \times 2^n \times 2^n$ equal area boxes [shown in Fig. 4(b) for $n = 3$] and calculating the fraction of boxes $\Phi_n(\theta_z,\theta_x)$ containing a portion of the exceptional set. For example, for the exceptional set corresponding to the protocol $(\theta_z,\theta_x) = (\pi/2,\pi/4)$ [Fig. 4(a)], Φ_3 is the number of black boxes in Fig. 4(c) divided by N. In this study, we use the fixed resolution $n = 6$, as demonstrated in Fig. 4(d). While higher resolutions yield better approximations, their computational cost is prohibitive when Φ_n is sampled across a 2D parameter space. Since n is kept fixed, for the remainder of this paper, we drop the subscript, i.e., $\Phi = \Phi_6$. A value of Φ close to 1 represents high coverage of the HS by $\bar{E}$ and, hence, a high degree of mixing. Conversely, a value of Φ close to 0 represents a low degree of mixing.

Sampling Φ in increments of $\pi/1800$ (0.1°) across the protocol space (θ_z,θ_x), Fig. 5 shows a complex distribution with many pronounced resonances (local minima, close to white) [25]. The most obvious structure is the symmetry across the line $\theta_x = \theta_z$. This is the result of the symmetry (A3) in Appendix A, which means that aside from a reflection, the protocol (θ_z,θ_x) with forward time and the protocol (θ_x,θ_z) with reverse time are identical. Therefore, invariant structures such as the exceptional set and cells are the same (up to symmetry) when the protocol order is reversed and, hence, Φ is also unchanged. In contrast, Juarez *et al.* [20] performed a similar quantitative analysis of mixing for the same PWI, measuring the degree of mixing by finding the center of mass of tracer particles initially evenly distributed in the $x < 0$, $y < 0$

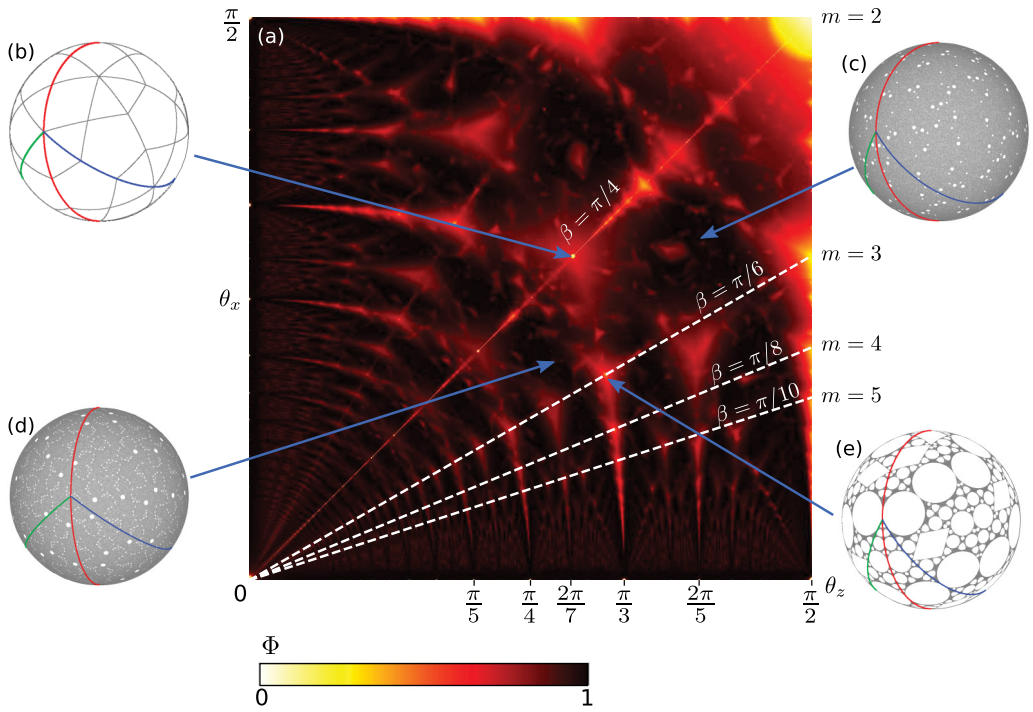

FIG. 5. (a) Distribution of Φ across the protocol space, sampled at increments of $\pi/1800$ in θ_z,θ_x. Φ is normalized such that zero coverage (white) corresponds to $\Phi = 0$, and complete coverage (black) corresponds to $\Phi = 1$. Lines of constant $\theta_x/\theta_z = \tan\beta$ are shown dashed white for $\beta = \pi/(2m), m = 3,4,5$. (b)–(e) Example exceptional sets corresponding to protocols indicated by blue arrows. (b), (e) Resonant protocols, i.e., local minima of Φ, where θ_z,θ_x are as in Figs. 3(b) and 3(c). (c), (d) Protocols with $\Phi \sim 1$: (c) $(\theta_z,\theta_x) = (1.25,0.93)$; (d) $(\theta_z,\theta_x) = (0.8,0.64)$.

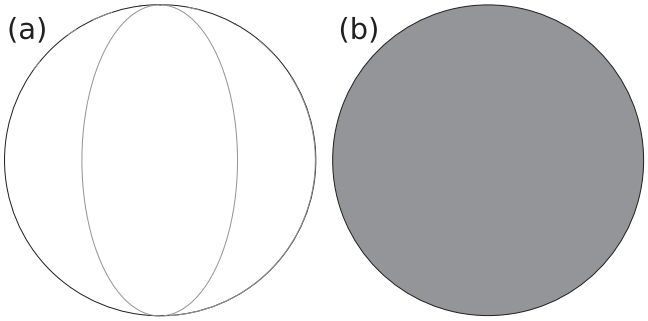

FIG. 6. Exceptional sets (gray) in the limit as $\theta_x \to 0$. (a) $\theta_z = \pi/3$. (b) $\theta_z = \pi/\pi$.

quarter-sphere as a function of the number of iterations, called the *segregation index*. Unlike Φ, the segregation index is not symmetric across the line $\theta_x = \theta_z$ because the forward time iterates of the protocols (θ_z,θ_x) and (θ_x,θ_z) are not connected via a symmetric relation, and the rotations of the HS about the z and x axes that comprise the BST PWI do not commute.

The corollary to the symmetry (A3) is that along the line $\theta_z = \theta_x$ the BST PWI possesses the reflection-reversal symmetry (A5) (see Appendix A), which means Lagrangian structures, e.g., cells and the exceptional set, must be symmetric about the plane $z = -x$. This additional constraint results in generally lower mixing efficacy compared to the rest of the protocol space; the median of Φ along $\theta_z = \theta_x$ is 0.528 which is much less than the median 0.952 across the entire protocol space.

We observe that the resonances with the least coverage of the exceptional set (closest to white) occur at intersections between lines of constant ratio $\theta_x/\theta_z = \tan\beta$, where $\beta = \pi/(2m)$, $m = 2,3,\ldots$ (white dashed lines in Fig. 5), and Arnold tongues that extend from values of θ_z commensurate with π (i.e., θ_z/π is rational) along the θ_z axis. To understand why these tongues exist, consider the limit as $\theta_x \to 0$. In this limit, the PWI becomes a rotation about the z axis only, with exceptional set

$$E = \bigcup_{k\in\mathbb{Z}} R^z_{(k\theta_z \bmod \pi)}\mathcal{C}, \tag{3}$$

where $\mathbb{Z}$ denotes the set of integers, R^z_γ denotes rotation by γ about the z axis, and $\mathcal{C}$ is the semicircle $x^2 + y^2 + z^2 = 1$, $y = 0$, $x < 0$. Even though there is an exceptional set and cutting occurs, no mixing occurs in this limit since cuts are always reconnected in the next iteration. When θ_z/π is rational, the union equation (3) consists of a finite number of disjoint arcs, e.g., Fig. 6(a) for $\theta_z = \pi/3$, and hence $\Phi = 0$. On the other hand, when θ_z/π is irrational, the curves $R^z_{(k\theta_z \bmod \pi)}\mathcal{C}$ for $k \in \mathbb{Z}$ are all disjoint and densely fill the HS, e.g., Fig. 6(b) for $\theta_z = \pi/\pi$, so that $\bar{E}$ covers the entire HS and $\Phi = 1$. Therefore, in the limit as $\theta_x \to 0$,

$$\Phi(\theta_z;\theta_x \to 0) = \begin{cases} 0, & \theta_z/\pi \in \mathbb{Q} \\ 1, & \theta_z/\pi \in \mathbb{R}\backslash\mathbb{Q} \end{cases} \tag{4}$$

where $\mathbb{Q}$ denotes the set of rational numbers, and $\mathbb{R}\backslash\mathbb{Q}$ denotes the set of real numbers excluding the rational numbers, i.e., the set of irrational numbers. Now, for small positive values of θ_x mode-locking-like phenomena occur, such that around each rational multiple of π, i.e., $\theta_z = \pi p/q$, there is a finite width interval with $\Phi(\theta_z;\theta_x) \sim 0$. This phenomenon is characterized by the existence of cells whose periods are multiples of q, and are robust under perturbations in θ_z. Understanding this mode-locking-like phenomenon allows us to rationalize the tongues observed in the distribution of the segregation index in a previous study [20]. However, a difference is that at small values of θ_x (and θ_z) the segregation index is generally large (indicating a low degree of mixing), and the tongues appear "fatter." This is because the segregation index in [20] was only computed over small numbers of iterations (10 and 25), and the mixing rate is generally slow at small values of θ_z,θ_x. On the other hand, Φ measures only the long-term mixing quality, and does not take into account the rate of mixing. Many thousands of iterations of the cutting lines $\mathcal{D}$ are required to produce good approximations of the exceptional set when θ_x is small, and it is expected that an almost identical tongue structure would be observed if the segregation index in [20] were computed using a similar number of iterations to that used here. Of course, for practical mixing applications, rapid mixing is desired, and short-term mixing quality is often a useful metric.

Similar mode-locking-like phenomena occur based on the ratio of θ_z and θ_x. In Appendix C, we consider the discrete BST PWI as the composition of continuous z- and x-axis rotations, prescribing the rotations an arbitrary fixed rotation rate ω. In other words, the z- and x-axis rotation maps are described as the integrals of rotational velocity fields for time periods $T_z = \theta_z/\omega$ and $T_x = \theta_x/\omega$. This enables us to consider the limit as $\theta_z,\theta_x \to 0$ with constant ratio θ_x/θ_z as the limit of infinitely fast switching between z- and x-axis rotation phases, i.e., $T_z,T_x \to 0$. In this limit, tracer particle trajectories are governed by a steady velocity field equivalent to rotation about the axis $(-\sin\beta,0,\cos\beta)$, where $\beta = \arctan(\theta_x/\theta_z)$. While particle motion in the interior of the HS is simple in the limit as $\theta_z,\theta_x \to 0$, the curves $\mathcal{D}_{1-3}$ and the atoms P_{2-4} all collapse onto the domain boundary ∂S, with multiple atoms collapsing onto some segments of ∂S. This means that multivalued periodic boundary conditions are produced, as described in Appendix C. When β/π is rational, particle trajectories are periodic, e.g., Figs. 14(a1) and (b1), whereas when β/π is irrational, particle trajectories densely fill the HS, e.g., Fig. 14(c1).

Away from the limit $\theta_z,\theta_x \to 0$, at small positive values of θ_z,θ_x, tracer particles loosely adhere to the streamlines of the steady velocity field in the limit $\theta_z,\theta_x \to 0$ [Figs. 14(a1), 14(b1), 14(c1) compared to Figs. 13(a2), 13(b2), and 13(c2)]. At small positive values of θ_z,θ_x, cells form chains that wrap around the HS, and the number of times they wrap around before returning to their initial position, termed the "wrapping multiplicity," is equal to the wrapping multiplicity of nearby orbits in the limit $\theta_z,\theta_x \to 0$. Hence, irrational values of β/π produce large wrapping multiplicities and small cells, whereas rational values of β/π, especially those with even denominators, produce small wrapping multiplicities and large cells (Appendix C). This behavior is not limited to small values of θ_z,θ_x, and is also evident at large values [Figs. 13(a3), 13(b3), 13(c3)], resulting in more prominent resonances along the white dashed lines $\beta = \pi/(2m)$, $m = 2,3,\ldots$, in Fig. 5.

Therefore, resonances result from a combination of two mode-locking-like phenomena. In Sec. III, these phenomena are discussed in more detail, and an analytic method for finding the resonances is introduced.

III. ANALYTIC MIXING PREDICTION

One approach to finding resonances is to compute the exceptional set and its coverage across the entire protocol space, like Fig. 5. However, this approach is computationally expensive and dependent on the resolution used to approximate Φ. Here, we devise an analytic method to find resonances in orientation-preserving PWIs based on finding the locations and sizes of cells, which are nonmixing regions.

The cells of interest here are those with maximum area that exist at the intersections of the mode-locking tongues that extend from the θ_z axis (characterized by the rational multiple of π from which the tongue extends, denoted p/q) and the lines of constant ratio θ_x/θ_z that correspond to different wrapping multiplicities (characterized by the number of times the chain of cells wraps around the HS, denoted m). For a chain of cells with $p = 1$, there are q cells per wrapping, and hence the chain has period mq. Each of these chains has one cell in the P_4 atom, with periodic itinerary $\mathcal{I}(m,q) = 41^{q-1}(21^{q-1})^{m-1}$, and the other cells in the chain have itineraries given by rotation permutations of this itinerary. For example, the cells in the period-6 chain (light red) in Fig. 3(c) have itineraries given by rotation permutations of $\mathcal{I}(2,3) = 41^2 21^2$. Based on Eq. (B5), each itinerary $\mathcal{I}(m,q)$ has a conjugate given by $\bar{\mathcal{I}}(m,q) = 321^{q-1}(21^{q-1})^{m-2}21^{q-2}$. Therefore, finding the location and size of one chain of cells also gives the size of its conjugate. The combined area of the cells with base itineraries $\mathcal{I}$ and $\bar{\mathcal{I}}$ provides a lower bound for the total area of all the cells in the HS, and hence upper bounds for Φ and the degree of mixing.

A. Cell location and size

For an orientation-preserving spherical PWI and any given itinerary, the periodic point at the center of the corresponding cell can be found by considering the net rotation over the full itinerary, as described by Scott *et al.* [15]. In each atom, the map M_{θ_z,θ_x} can be expressed as the composition of two rotations:

$$P_1 : R_1 = R^x_{\theta_x} R^z_{\theta_z}, \tag{5}$$

$$P_2 : R_2 = R^x_{\theta_x} R^z_{\theta_z+\pi}, \tag{6}$$

$$P_3 : R_3 = R^x_{\theta_x+\pi} R^z_{\theta_z}, \tag{7}$$

$$P_4 : R_4 = R^x_{\theta_x+\pi} R^z_{\theta_z+\pi}. \tag{8}$$

Over a full itinerary, the net rotation is the composition of these atomic rotations. For example, for the itinerary 41^2 the net rotation is $R_{41^2} = R_1 R_1 R_4$, noting that the rightmost rotation is performed first. Finding the normalized axis of the net rotation gives two points $\pm\boldsymbol{v}$ on the unit sphere, with at least one on the HS, that are invariant under the net rotation, and hence periodic points. Whichever of $\pm\boldsymbol{v}$ is on the HS is the center of the cell. For instance, for the itinerary 41^2 the center is $\boldsymbol{x} = \hat{\boldsymbol{a}}$ where $\boldsymbol{a} = (a_1,a_2,a_3)$ and

$$\begin{aligned} a_1 &= \cos\frac{\theta_x}{2}\sin\frac{\theta_z}{2}[2+\cos\theta_z-\cos\theta_x(\cos\theta_z+1)],\\ a_2 &= \cos\frac{\theta_x}{2}\cos\frac{\theta_z}{2}[\cos(\theta_x)+\cos\theta_z(\cos\theta_x-1)],\\ a_3 &= \sin\frac{\theta_x}{2}\cos\frac{\theta_z}{2}[\cos\theta_z+\cos\theta_x(\cos\theta_z+1)]. \end{aligned} \tag{9}$$

Note that the axis of net rotation can be found for any itinerary, but if $\pm\boldsymbol{v}$ are outside the first atom of the itinerary, then the center of the cell must be outside the atom in which the cell is assumed to exist, a contradiction. Hence, the cell does not exist. For example, for some values of θ_z,θ_x the axis of rotation for the 41^2 itinerary is outside P_4, which is a contradiction to the assumption that the itinerary starts in P_4. Therefore, in addition to determining the center of cells when they do exist, this method also indicates when cells with a given itinerary do not exist.

Once the center $\boldsymbol{v}$ of a period-n cell has been found, its radius is determined as

$$r = \min_{0\leqslant i<n,\ \mathcal{C}\in\{\mathcal{D}_{1-3},\partial S\}} d\left(M^i_{\theta_z,\theta_x}(\boldsymbol{v}),\mathcal{C}\right), \tag{10}$$

where $d(\boldsymbol{x},\mathcal{C})$ is the shortest distance from the point $\boldsymbol{x}$ to the curve $\mathcal{C}$. In other words, the cell radius is the minimum of all the distances from the centers of the cells in the chain, $M^i_{\theta_z,\theta_x}(\boldsymbol{v})$, to the nearest cutting line or domain boundary. For example, in Fig. 3(a) the radii of the cells in the chain with base itinerary 41^2 (dark red) are all equal to the distance from the center of the cell in P_4 to $\mathcal{D}_1$, the red cutting line. Note that when the cell is a regular polygon, e.g., the pentagons in Fig. 3(b), r is the inradius (apothem), i.e., the radius of the largest circle that can be wholly contained within the polygon, rather than the circumradius (distance from the center to a vertex). To find $d(\boldsymbol{x},\mathcal{C})$, for $\mathcal{C}\in\{\mathcal{D}_{1-3},\partial S\}$, we note that the cutting lines $\mathcal{D}_{1-3}$ and domain boundary ∂S are all segments of great circles [i.e., the intersection of the unit sphere with planes $\mathcal{P}(\mathcal{C})$ that pass through the sphere origin]. Each great circle $\mathcal{C}$ is characterized by the vector $\boldsymbol{n}(\mathcal{C})$ normal to its plane $\mathcal{P}(\mathcal{C})$ (choosing an orientation for $\mathcal{C}$). For $\mathcal{C}\in\{\mathcal{D}_{1-3},\partial S\}$, these normals are given by

$$\boldsymbol{n}(\mathcal{D}_1) = (\sin\theta_z, -\cos\theta_z, 0), \tag{11}$$

$$\boldsymbol{n}(\mathcal{D}_2) = (\cos\theta_x\sin\theta_z, -\cos\theta_x\cos\theta_z, \sin\theta_x), \tag{12}$$

$$\boldsymbol{n}(\mathcal{D}_3) = (\cos\theta_x\sin\theta_z, -\cos\theta_x\cos\theta_z, -\sin\theta_x), \tag{13}$$

$$\boldsymbol{n}(\partial S) = (0,1,0). \tag{14}$$

Since the geodesic distance along the unit sphere between a point $\boldsymbol{x}$ and the normal $\boldsymbol{n}(\mathcal{C})$ equals the angle between them, $\arccos[\boldsymbol{x}\cdot\boldsymbol{n}(\mathcal{C})]$, it follows that the distance from any point $\boldsymbol{x}$ on the HS to a great circle $\mathcal{C}$ with normal $\boldsymbol{n}(\mathcal{C})$ is

$$d(\boldsymbol{x},\mathcal{C}) = \frac{\pi}{2} - \arccos[\boldsymbol{x}\cdot\boldsymbol{n}(\mathcal{C})]. \tag{15}$$

Furthermore, the sign of d determines which side of $\mathcal{C}$ the point is on, which can be used for the great circles $\mathcal{D}_{1-3}$ and ∂S to determine which atom $\boldsymbol{x}$ is in, and hence whether or not a cell with a given itinerary exists. For example, if $d(\boldsymbol{x},\mathcal{D}_1) > 0$,

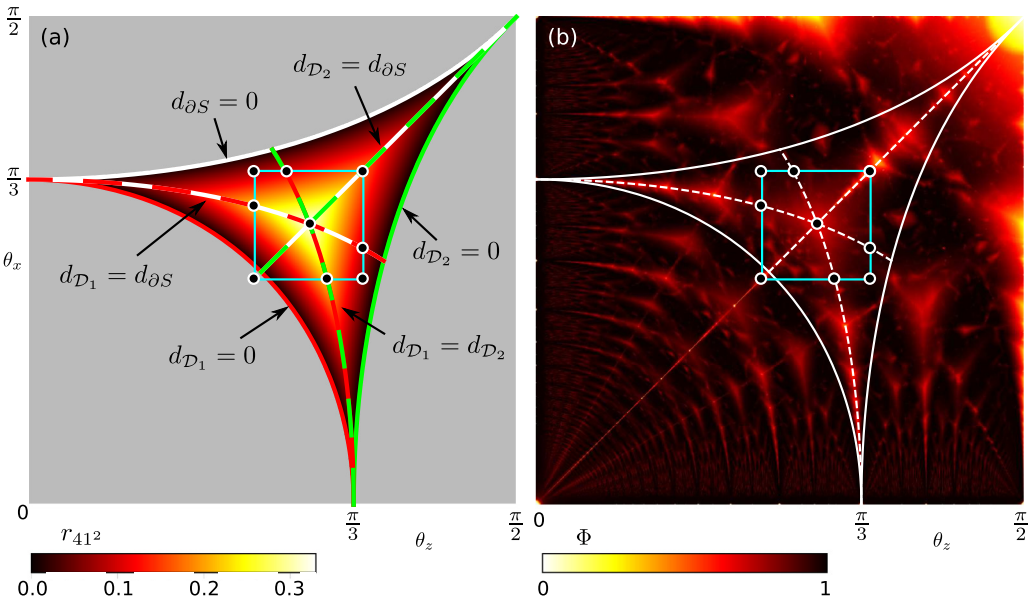

FIG. 7. (a) Radius of cells with base itinerary 41^2, r_{41^2}, from Eq. (16). The cell does not exist in the gray region beyond the solid red, green, and white annihilation boundaries, which satisfy Eqs. (21)–(23) (denoting $d(\boldsymbol{x},\mathcal{C})$ by $d_{\mathcal{C}}$ for short). The dashed red and green, red and white, and green and white curves represent protocols where the center of the cell is equidistant to two of the boundaries, given by Eqs. (17)–(19), e.g., cell centers for protocols along the red and green curve are equidistant to $\mathcal{D}_1$ and $\mathcal{D}_2$ ($d_{\mathcal{D}_1} = d_{\mathcal{D}_2}$). The protocol where all three dashed curves intersect, $\theta_z = \theta_x = \theta^* = \arccos[(-1+\sqrt{5})/2] \approx 0.9046 \approx 51.83^\circ$, has maximal cell radius [see Fig. 3(b)]. Exceptional sets for the white-outlined black points on the blue-sided square with side length $\pi/9$ centered on the maximal protocol are shown in Fig. 8. (b) The distribution of Φ from Fig. 5 overlayed with the annihilation boundaries (solid) and equidistance curves (dashed) for the 41^2 itinerary.

then $\boldsymbol{x}$ must be in P_1 or P_3 [the atoms on the right of $\mathcal{D}_1$ in Fig. 2(a)]; if $d(\boldsymbol{x},\mathcal{D}_1) < 0$, then $\boldsymbol{x}$ must be in P_2 or P_4 [the atoms on the left of $\mathcal{D}_1$ in Fig. 2(a)]; and, if $d(\boldsymbol{x},\mathcal{D}_1) = 0$, then $\boldsymbol{x}$ must be on $\mathcal{D}_1$.

Using the period-3 itinerary 41^2 as an example, demonstrated by the dark red cells in Fig. 3, we observe that the cell in P_4 always forms the tangent intersection to $\mathcal{D}$ or ∂S, and hence determines the size of all the cells in the chain. Letting $\boldsymbol{x} = \hat{\boldsymbol{a}}$ [Eq. (9)] denote the center of the cell in P_4, the cell's radius equals the minimum of the distances of the center to the three boundaries of P_4:

$$r_{41^2}(\theta_z,\theta_x) = \min\left[d(\boldsymbol{x},\mathcal{D}_1), d(\boldsymbol{x},\mathcal{D}_2), d(\boldsymbol{x},\partial S)\right]. \tag{16}$$

This radius is shown as a contour plot in Fig. 7(a) across the protocol space θ_z,θ_x. The dashed curves indicate protocols for which the cell center is equidistant to two of $\mathcal{D}_1$, $\mathcal{D}_2$ or ∂S, i.e.,

$$\begin{aligned} d(\boldsymbol{x},\mathcal{D}_1) = d(\boldsymbol{x},\mathcal{D}_2) &\iff \boldsymbol{x}\cdot\boldsymbol{n}(\mathcal{D}_1) = -\boldsymbol{x}\cdot\boldsymbol{n}(\mathcal{D}_2) \\ &\iff \cos\theta_z = \frac{1}{1+\cos\theta_x}, \end{aligned} \tag{17}$$

$$\begin{aligned} d(\boldsymbol{x},\mathcal{D}_1) = d(\boldsymbol{x},\partial S) &\iff \boldsymbol{x}\cdot\boldsymbol{n}(\mathcal{D}_1) = \boldsymbol{x}\cdot\boldsymbol{n}(\partial S) \\ &\iff \cos\theta_x = \frac{1}{1+\cos\theta_z}, \end{aligned} \tag{18}$$

$$\begin{aligned} d(\boldsymbol{x},\mathcal{D}_2) = d(\boldsymbol{x},\partial S) &\iff \boldsymbol{x}\cdot\boldsymbol{n}(\mathcal{D}_2) = -\boldsymbol{x}\cdot\boldsymbol{n}(\partial S) \\ &\iff \theta_x = \theta_z, \end{aligned} \tag{19}$$

where the negative signs result from the relative orientations of $\boldsymbol{n}(\mathcal{D}_1),\boldsymbol{n}(\mathcal{D}_2),\boldsymbol{n}(\partial S)$. Examples of exceptional sets along these curves are shown in Figs. 8(b)–8(f), and 8(h), corresponding to the protocols marked by white-outlined black circles in Fig. 7. The cells with itinerary 41^2 (dark red) are larger when the cell in P_4 touches two boundaries [Figs. 8(c), 8(d), and 8(h)] compared to one [Figs. 8(a), 8(b), 8(f), and 8(i)], and the cells are largest when the cell in P_4 touches all three boundaries [Fig. 8(e)], which occurs when all three equidistance curves intersect: $\theta_z = \theta_x = \theta^* = \arccos[(-1+\sqrt{5})/2] \approx 0.9046 \approx 51.83^\circ$, corresponding to the maximum radius $r_{41^2} \approx 0.3309$. At this maximal protocol the entire domain, including the exceptional set, is periodic, and the cells form a polygonal tiling of the HS. The 41^2 chain of cells and its conjugate 321 are regular spherical pentagons, with internal rotation equal to $4\pi/5$, that form a band around the center of the HS. All other cells are irregular polygons, with zero internal rotation. Therefore, $\Phi = 0$ for this maximal protocol, and hence it is a resonance. Moving away from the maximal protocol in any direction, the cell shrinks, and eventually annihilates when its center meets one of $\mathcal{D}_{1,2}$, ∂S, as in Fig. 8(g). The curves where the cell annihilates, called "annihilation boundaries," are shown as solid red, green, and white in Fig. 7(a), corresponding to the curves

$$[d(\boldsymbol{x},\mathcal{C}) = 0 \iff \boldsymbol{x}\cdot\boldsymbol{n}(\mathcal{C}) = 0] \quad \text{for} \quad \mathcal{C} = \mathcal{D}_{1,2}, \partial S. \tag{20}$$

For the 41^2 itinerary, the equations for these boundaries can be simplified using Eqs. (9) and (11)–(14):

$$\mathcal{C} = \mathcal{D}_1: \quad \cos\theta_x = \frac{2-\cos\theta_z}{1+\cos\theta_z}, \tag{21}$$

$$\mathcal{C} = \mathcal{D}_2: \quad \cos\theta_z = \frac{\cos\theta_x}{1+\cos\theta_x}, \tag{22}$$

$$\mathcal{C} = \partial S: \quad \cos\theta_x = \frac{\cos\theta_z}{1+\cos\theta_z}. \tag{23}$$

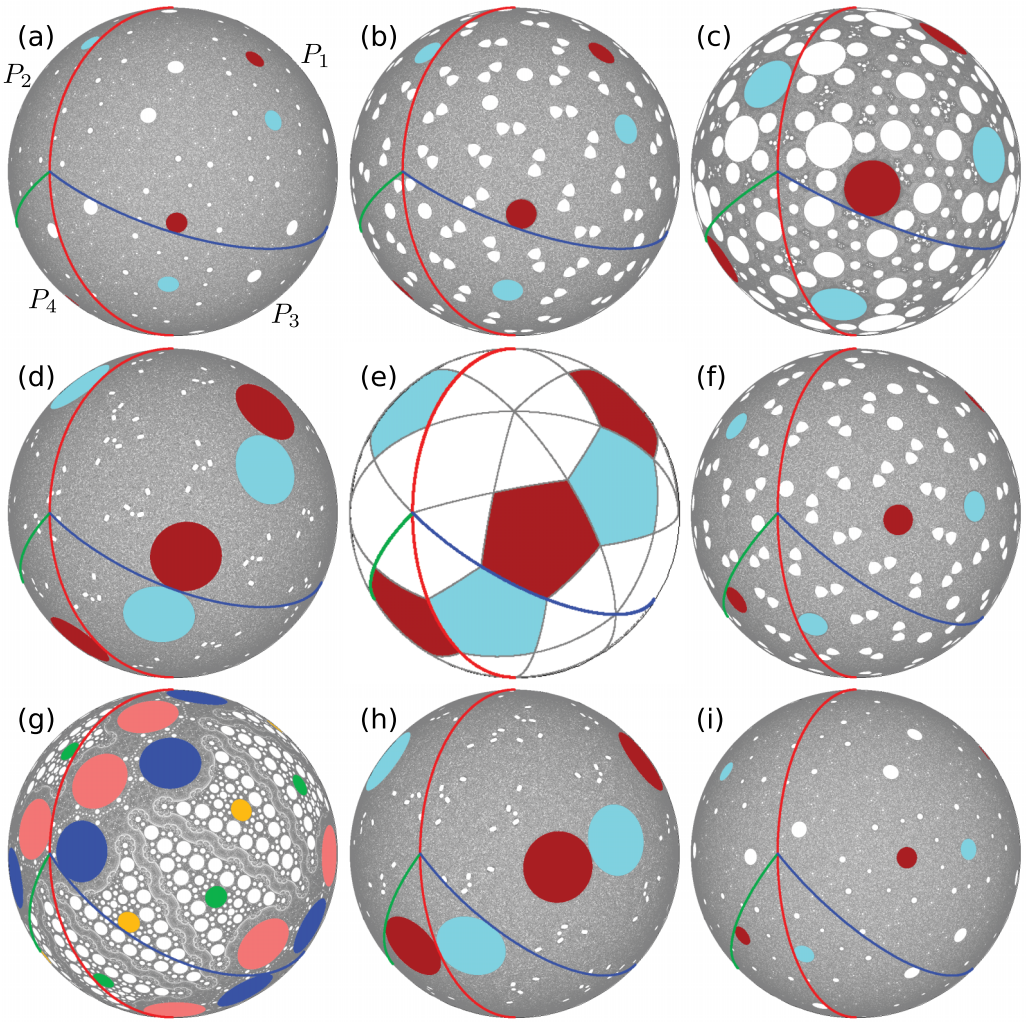

FIG. 8. Exceptional sets for the protocols marked by white-outlined black circles on the blue-sided square in Fig. 7. Cells with base itinerary 41^2 are dark red; conjugate cells with base itinerary 321 are light blue. The cell with itinerary 41^2 in P_4 touches one boundary in (a), (b), (f), (i); two boundaries in (c), (d), (h); and all three boundaries in (e), corresponding to the resonance $\theta_z = \theta_x = \theta^* = \arccos[(-1+\sqrt{5})/2]$. Note that the cell with itinerary 41^2 in P_4 is difficult to see when viewing the HS from below in (a) and (b), as it is close to the boundary ∂S and has small radius. In (g) no cell with itinerary 41^2 exists, period-4 cells with base itinerary 41^3 are orange, and their conjugate cells (itinerary 321^2) are green; period-6 cells with base itineraries 21^231^2 and 2131^3 are light red and dark blue, respectively. Protocols (θ_z,θ_x) are (a) $(\theta^* - \pi/18, \theta^* + \pi/18)$, (b) $(0.8243, \theta^* + \pi/18)$ (approximate values correspond to intersections between equidistant curves and the blue-sided square in Fig. 7), (c) $(\theta^* + \pi/18, \theta^* + \pi/18)$, (d) $(\theta^* - \pi/18, 0.9607)$, (e) (θ^*, θ^*), (f) $(\theta^* + \pi/18, 0.8243)$, (g) $(\theta^* - \pi/18, \theta^* - \pi/18)$, (h) $(0.9607, \theta^* - \pi/18)$, (i) $(\theta^* + \pi/18, \theta^* - \pi/18)$.

Beyond these boundaries (in the gray regions), the center of the cell is outside P_4 and hence the cell does not exist.

Considering the link between the size of the 41^2 cell and the mode-locking-like phenomena, Fig. 7(b) shows that the shape of the annihilation boundaries captures the general shape of the tongue extending from $\theta_z = \pi/3$, and also shows that the dashed equidistance curve Eq. (17) passes through all the resonances along the tongue. Therefore, finding these relatively simple properties of the 41^2 cell reveals significant information about the system as a whole, including a resonant protocol such that the entire domain is periodic. In Sec. III B, more resonances are detected and protocols with high mixing efficacy are predicted by considering a range of itineraries, in particular those of the form $\mathcal{I}(m,q)$.

B. An analytic picture of resonances

Like the 41^2 itinerary, for all itineraries $\mathcal{I}(m,q)$ the cell that determines the size of all the cells in the chain is located in P_4, and hence the radius is given by Eq. (16). Therefore, the annihilation boundaries and equidistance curves also take the form (17)–(20). These are shown in Fig. 9 for several m and q values. As for the 41^2 itinerary in Fig. 7(b), the annihilation boundaries capture the general shape of the tongues, and meet at cusps at rational multiples of π in the limit $\theta_x \to 0$. The resonances (local minima of Φ) coincide exactly with the protocols where cells are equidistant from three boundaries, i.e., the intersections of the dashed curves of the same color in Fig. 9. Therefore, the resonances can be found by solving Eqs. (17)–(19) simultaneously. While this can be solved analytically for the 41^2 itinerary, for longer

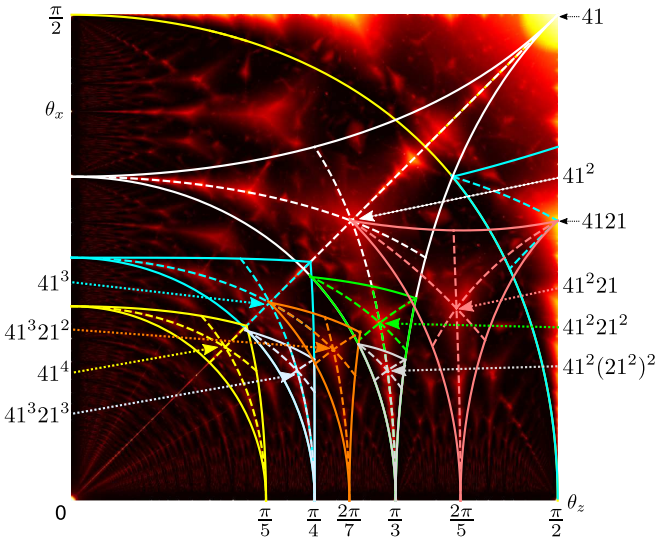

FIG. 9. Distribution of Φ from Fig. 5 shown with annihilation boundaries (solid) and equidistance curves (dashed) for 10 low-period itineraries (different colors). The resonances (local minima in Φ) occur at protocols where all three equidistance curves of an itinerary meet, and are labeled for each itinerary by dotted arrows.

itineraries an analytic solution does not generally exist, and numeric root finding is used instead. In any case, the protocols at local minima in mixing efficacy across the protocol space can be found without needing to compute the exceptional set and its fraction of coverage.

Furthermore, the annihilation boundaries corresponding to $\mathcal{D}_{1,2}$ and the equidistance curve (17) coincide for the itineraries $41^2, 41^2 21^2, 41^2(21^2)^2$ (white, green, gray), i.e., $\mathcal{I}(m,q)$ for $q = 3$, $m = 1,2,3$. In Appendix D, we show that this coincidence of curves occurs for all m at each value of q because the centers of cells corresponding to a fixed value of q lie on a great circle that also passes through the point where the cutting lines $\mathcal{D}_{1-3}$ meet. Hence, all the cells annihilate simultaneously and become equidistant to $\mathcal{D}_1$ and $\mathcal{D}_2$ simultaneously.

The corresponding exceptional sets for the low-period resonant protocols are shown in Fig. 10, arranged by the wrapping multiplicity m and the rational multiple ($\theta_z^*/\pi = p/q$) from which the corresponding tongue extends. For each single-wrap resonance ($m = 1$), the domain is entirely periodic, and the exceptional set forms a polygonal tiling of the HS consisting of regular $(2q-1)$-gons, irregular triangles, and irregular quadrilaterals. Therefore, when $m = 1$, the domain as a whole will periodically disassemble and reassemble as the cells are shuffled around, with reassembly period given by the lowest common multiple of all the periodicities of the cells. At all other values of m the cells are circles, meaning the exceptional set is a fat fractal, and there are (small) positive area regions where mixing occurs. Furthermore, the disassembly and reassembly of cells is such that even the region consisting of all cells will never return to its initial configuration when $m \neq 1$. This is because each cell has an irrational internal rotation angle α, and there are arbitrarily small cells with arbitrarily long periods, meaning a lowest common multiple of periodicities does not exist. Therefore, when $m \neq 1$ some mixing can occur in the small mixing region and via cell disassembly, but the degree of mixing is relatively low compared to nonresonant protocols.

In contrast to the resonances that occur on the tongues with $\theta_z^* = \pi/q$, the resonances at $2\pi/7$ and $2\pi/5$ produce significantly better mixing (third and fifth columns in Fig. 10), and we expect similar phenomena for resonances corresponding to $\theta_z^* = 2\pi/q$ with $q = 9,11,\ldots$. Since resonant cells along each tongue have period $m\pi/\theta_z^*$ where m is the wrapping multiplicity [e.g., for $\theta_z^* = \pi/4$ the periods are $4m$ (second column in Fig. 10)] for $\theta_z^* = 2\pi/q$ with $q = 5,7,\ldots$, the resonant cells only exist when m is even. For example, for $\theta_z^* = 2\pi/5$ and wrapping multiplicity $m = 2$, the resonant cell is period 5 and wraps around the HS twice (fifth column of Fig. 10). It is impossible for a single wrapping ($m = 1$) to exist for $\theta_z^* = 2\pi/5$, as it would have period 5/2, and the same situation would occur for any odd wrapping multiplicity. By observing the resonant cells and their itineraries for cases with $\theta_z^* = \pi p/q$ and $p \neq 1$, the family of itineraries $\mathcal{I}(m,q)$ can be extended, such that the itinerary of the resonant cell with wrapping multiplicity m and period mq/p is

$$\mathcal{I}(m,q/p) = 41^{a-1}(21^{a-1})^{p-b-1}(21^{a-2})^{b} \times [(21^{a-1})^{p-b}(21^{a-2})^{b}]^{m/p-1}, \quad (24)$$

where $q = ap - b$, $a = \lceil q/p \rceil$ is the ceiling of q/p, i.e., the smallest integer greater than q/p, and $-b \equiv q \bmod p$, with $b \in \{0,1,\ldots,p-1\}$. For example, $\mathcal{I}(2,5/2) = 41^2 21$, and in this case the exceptional set almost entirely fills the HS excluding the resonant cells and their conjugate (dark red and light blue) (fifth column in Fig. 10). The annihilation boundaries and equidistance curves for the itinerary $\mathcal{I}(2,5/2) = 41^2 21$ are shown in pink in Fig. 9. Compared to the other resonant protocols with wrapping multiplicity $m = 2$, the resonance corresponding to the itinerary $41^2 21$ is relatively far from the line $\beta = \pi/6$ in Fig. 5 because the cell that forms the tangent intersection to one of the cutting boundaries is not always in P_4. For some protocols, the size-limiting cell is in P_1. Therefore, the annihilation boundaries and equidistance curves are not given by Eqs. (17)–(20), instead the cells in P_4 and P_1 that limit the size both need to be taken into account. The same is true for other itineraries of the form $\mathcal{I}(m,q/p)$ with $p \neq 1$ such as the period-7 itinerary $\mathcal{I}(2,7/2) = 41^3 21^2$ on the line $\beta = \pi/6$ in Fig. 5, whose annihilation boundaries and equidistance curves are shown in orange in Fig. 9.

C. Predicting mixing

By finding resonances, i.e., protocols at local minima in mixing efficacy, we can eliminate regions of the protocol space known to yield low degrees of mixing, and hence predict regions where a high degree of mixing is likely. In the regions of the protocol space outside the annihilation boundaries [Fig. 11(a)], we can guarantee that no cells exist for the itineraries shown in Fig. 9. Furthermore, in the two regions indicated by arrows in Fig. 11(a), it can be shown that no cells with itinerary $\mathcal{I}(m,q/p)$ exist for any values of m, p, and q. For protocols in these two regions, cells exist with itineraries not of the form $\mathcal{I}(m,q/p)$, and it is possible that these cells could be large and inhibit mixing, or many small cells could tightly pack the HS resulting in low

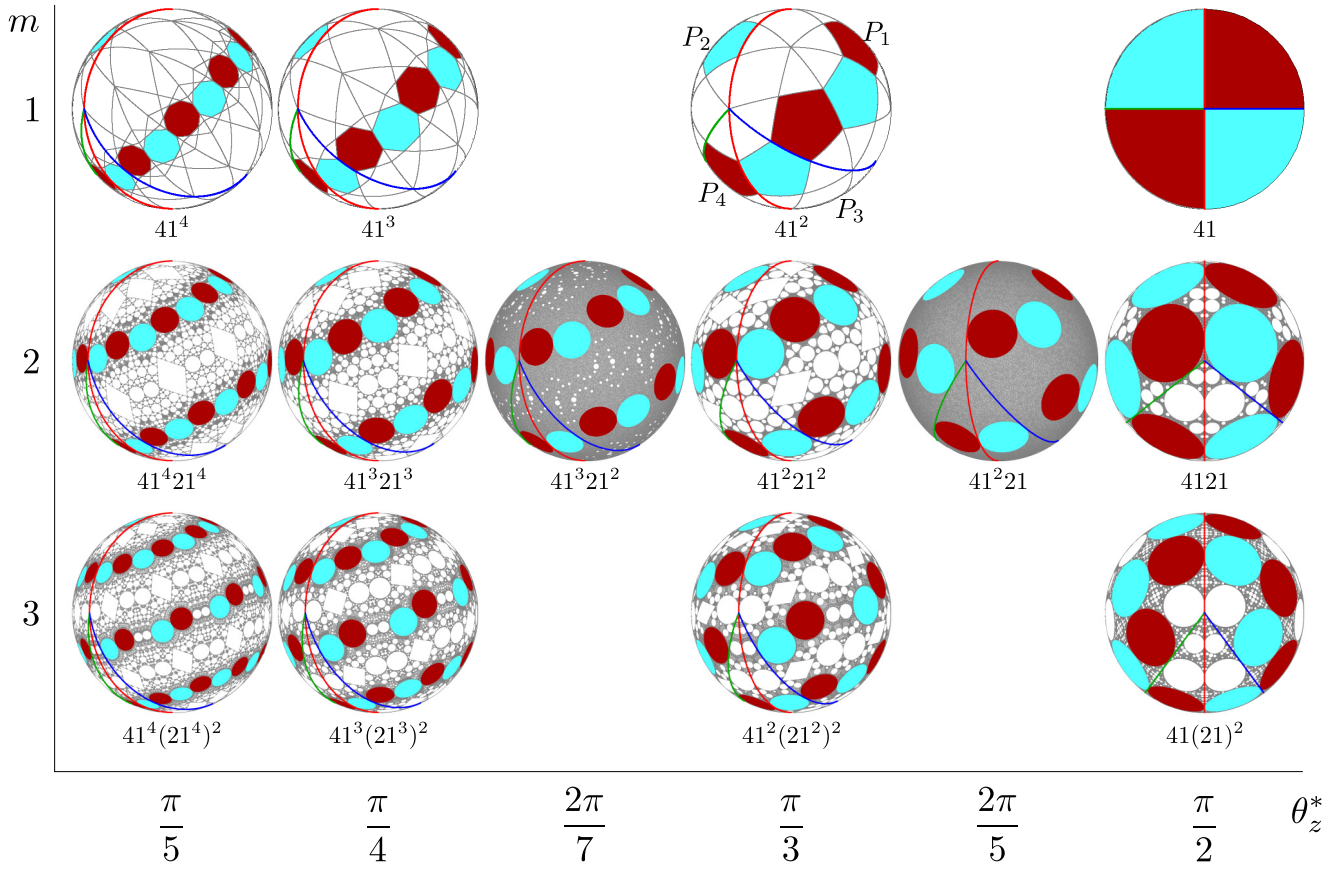

FIG. 10. Exceptional sets of the BST PWI for resonant protocols. For each resonance the corresponding itinerary that is tangent to three boundaries is indicated, its cells are colored dark red, and the cells of the conjugate itinerary are colored light blue. The θ_z^* axis represents the rational multiple of π that the resonance is attached to via the tongues, and m is the wrapping multiplicity of the resonant itinerary.

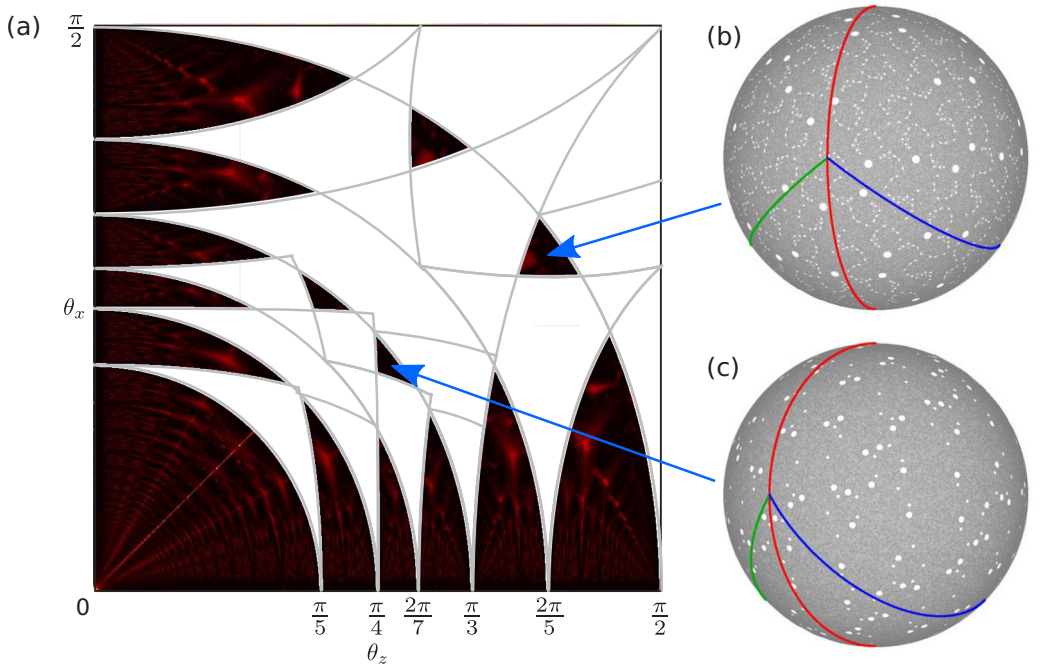

FIG. 11. (a) Distribution of Φ (Fig. 5) with regions containing cells corresponding to the itineraries in Fig. 9 colored white (and their reflection across the line $\theta_z = \theta_x$). Annihilation boundaries for the itineraries are shown in gray. (b), (c) Exceptional sets outside the annihilation boundaries that are predicted to produce a high degree of mixing. (b) $(\theta_z,\theta_x) = (1.25,0.93)$. (c) $(\theta_z,\theta_x) = (0.8,0.64)$.

coverage by the exceptional set. However, we observe that Φ is in general much lower within the annihilation boundaries of the itineraries $\mathcal{I}(m,q/p)$ than the two regions indicated in Fig. 11(a), confirming that mixing efficacy is generally higher in the region outside the annihilation boundaries. Considering the two specific protocols indicated by the arrows in Fig. 11(a), the corresponding exceptional sets [Figs. 11(b) and 11(c)] have some small high-period cells, but the exceptional set covers a large portion of the domain, indicating a high degree of mixing.

Therefore, by finding the annihilation boundaries and equidistance curves of only a few low-period itineraries belonging to the family $\mathcal{I}(m,q/p)$, we are able to determine regions of the protocol space at local minima in mixing efficacy and even predict regions of high mixing efficacy. Of course, some regions of relatively low mixing efficacy are still evident in the remaining colored portions of Fig. 11. For instance, light regions along the lines $m = 4,5$ (see Fig. 5) remain. However, a similar approach to that used so far could be used to eliminate these regions from Fig. 11. In any case, compared to numerical evaluation of Φ across the entire protocol space, this method is less computationally expensive, and provides insight into the mechanisms that drive mixing and periodicity, including mode-locking-like phenomena.

IV. CONCLUSIONS

By finding the locations and radii of cells, resonances that correspond to protocols at local minima in mixing efficacy can be found analytically, and protocols that yield a high degree of mixing can be predicted. In orientation-preserving spherical PWIs this can be achieved by considering the net rotation produced by the PWI map over the course of a periodic itinerary. Each cell has a unique periodic itinerary, which specifies the sequence of isometries that it undergoes, and hence determines its center and radius. By considering properties of the PWI, such as symmetries and the limits as parameters approach zero, a family of itineraries that control the resonances may be found. This is the case for the BST PWI, where the itineraries $\mathcal{I}(m,q/p)$ control the low-order resonances. However, more generally, such a family of itineraries may not exist. In those cases, the resonances can still be predicted analytically by considering a larger number of itineraries, and combining the areas of cells to form a lower bound for the total area of all cells. It has been demonstrated for a different spherical PWI that high-period cells generally have a smaller radius [15]. Hence, it appears best to consider the lowest period cells (with shortest itineraries) first.

Since these mixing predictions are based on invariant structures such as cells and the exceptional set, only long-term mixing quality can be predicted. In practical applications, the rate of mixing is often of equal, if not greater, importance to the ultimate effectiveness of a mixing protocol. Future work should focus on the links between resonances and the rate of mixing. It is anticipated that additional factors such as the relative magnitudes of θ_z and θ_x, or other metrics such as the amount of mixing per net rotation in the protocol (i.e., $\theta_z + \theta_x$), will also need to be considered to be able to predict good, rapid mixing.

While the methods used here apply to orientation-preserving spherical PWIs, i.e., those only consisting of rotation transformations, the inclusion of orientation-reversing transformations, i.e., reflections, does not significantly change dynamics, and the method can be adapted to these cases. If M is an orientation-reversing map, then $S \circ M$ is orientation preserving, where S is any reflection transformation. Therefore, the method used here can be applied to find cell centers $\boldsymbol{x}$ for $S \circ M$, which can then be reflected, $S^{-1}(\boldsymbol{x})$, to produce cell centers for M.

In experiments using the granular BST flow, Zaman *et al.* [8] have shown that the BST PWI forms a kinematic "skeleton," and that sufficiently large cells can survive even when stretching in the flowing layer and collisional diffusion are present. These cells yield "sticky" regions where particles tend to spend long periods of time (and hence, do not mix). By finding a threshold cell radius, above which cells produce sticky regions in experiment, the analytic description of cell radius found here can be immediately applied to find all the regions of the protocol space where sticky regions will exist in experiment.

The BST PWI admits a number of generalizations that could lead to new and interesting phenomena. Allowing nonperpendicular rotation axes breaks some symmetries and adds a third parameter to the system. Such a system is still an orientation-preserving spherical PWI. Hence, resonances, annihilation boundaries, and equidistance surfaces can be found in the 3D protocol space. Considering the PWI as the limit of granular tumbler flow [8], another generalization is to change the fill fraction of the sphere. When the sphere is not half-full, the corresponding map is no longer a PWI, and particle motion is generated by a combination of stretching-and-folding and cutting-and-shuffling actions. This simple change greatly adds to the complexity of the system. Understanding the interplay between stretching-and-folding and cutting-and-shuffling motions in the non-half-full cases could provide insights into the mechanics and mathematics of mixing in more general and practical scenarios, for instance, nonspherical geometries such as a V-blender [4–6].

Future work should also focus on understanding and classifying the polygonal tilings that are produced by the BST PWI. The family of polygonal tilings produced by the BST PWI may be a novel class of polygonal tiling of the HS, and other spherical PWIs could produce new families of polygonal tilings. However, it is difficult to predict whether a given spherical PWI is even capable of producing polygonal tilings, let alone to predict what they would look like.

ACKNOWLEDGMENT

P. Park was supported by the National Science Foundation Contract No. CMMI-1435065.

APPENDIX A: SYMMETRIES

Symmetries of time-periodic flows provide insights into their Lagrangian topologies, and have been exploited to better understand many 2D [26–29] and 3D [30–32] systems. The BST PWI possesses a number of symmetries that control its Lagrangian topology. The map can be written as the composition of z- and x-axis rotations, i.e., $M_{\alpha,\beta} = \tilde{M}^x_\beta \tilde{M}^z_\alpha$, where $\theta_z = \alpha$, $\theta_x = \beta$, and $\tilde{M}$ is used to denote rotation

modulo π. Since the x-axis rotation can be written as the conjugation of the z-axis rotation with a rotation about the y axis, i.e., $\tilde{M}^x_\beta = R^y_{-\pi/2}\tilde{M}^z_\beta R^y_{\pi/2}$, the BST PWI can be written as $M_{\alpha,\beta} = R^y_{-\pi/2}\tilde{M}^z_\beta R^y_{\pi/2}\tilde{M}^z_\alpha$. By writing the map in this form, the symmetries of the z-axis rotation can be used to derive symmetries of the BST PWI.

The z-axis rotation possesses two symmetries, first the reflection-reversal symmetry

$$\tilde{M}^z_\theta = S_{yz}\left(\tilde{M}^z_\theta\right)^{-1}S_{yz}, \tag{A1}$$

where $S_{yz} : (x,y,z) \mapsto (-x,y,z)$ denotes reflection through the yz plane. The z-axis rotation also has the reflection symmetry

$$\tilde{M}^z_\theta = S_{xy}\tilde{M}^z_\theta S_{xy}, \tag{A2}$$

where S_{xy} denotes reflection through the xy plane.

Deriving from Eq. (A1), the BST PWI has the following symmetry that relates the protocols (α,β) and (β,α):

$$\begin{aligned} M_{\alpha,\beta} &= R^y_{-\pi/2}\tilde{M}^z_\beta R^y_{\pi/2}\tilde{M}^z_\alpha \\ &= R^y_{-\pi/2}\left[S_{yz}\left(\tilde{M}^z_\beta\right)^{-1}S_{yz}\right]R^y_{\pi/2}\left[S_{yz}\left(\tilde{M}^z_\alpha\right)^{-1}S_{yz}\right] \\ &= S_1\left(\tilde{M}^z_\beta\right)^{-1}S_1^{-1}S_{yz}\left(\tilde{M}^z_\alpha\right)^{-1}S_{yz} \\ &= S_1\left(\tilde{M}^z_\beta\right)^{-1}R^y_{-\pi/2}\left(\tilde{M}^z_\alpha\right)^{-1}R^y_{\pi/2}S_1 \\ &= S_1 M^{-1}_{\beta,\alpha}S_1, \end{aligned} \tag{A3}$$

where $S_1 = R^y_{-\pi/2}S_{yz} : (x,y,z) \mapsto (-z,y,-x)$ denotes reflection through the plane $z = -x$. This means that the (α,β) protocol is the reflection through the $z = -x$ plane of the reverse time (β,α) protocol. Therefore, when the order of the rotation angles is changed, all invariant structures such as cells and the exceptional set occur as reflections of one another through the plane $z = -x$. For instance, for a period-n point $\boldsymbol{x}$ of $M_{\alpha,\beta}$ it follows that

$$\boldsymbol{x} = M^n_{\alpha,\beta}(\boldsymbol{x}) = \left(S_1 M^{-1}_{\beta,\alpha}S_1\right)^n(\boldsymbol{x}) = S_1 M^{-n}_{\beta,\alpha}S_1(\boldsymbol{x}), \tag{A4}$$

and hence $S_1(\boldsymbol{x})$ is a period-n point of $M_{\beta,\alpha}$.

As a corollary to the symmetry (A3), when the rotation angles are equal (i.e., $\alpha = \beta$) the flow possesses the reflection-reversal symmetry

$$M_{\alpha,\alpha} = S_1 M^{-1}_{\alpha,\alpha}S_1. \tag{A5}$$

This means that invariant structures (cells, periodic points, the exceptional set, etc.) must occur symmetrically about the plane $z = -x$.

As a result of the reflection symmetry (A2), the BST PWI has the symmetry

$$\begin{aligned} M_{\alpha,\beta} &= R^y_{-\pi/2}\tilde{M}^z_\beta R^y_{\pi/2}\tilde{M}^z_\alpha \\ &= R^y_{-\pi/2}\left[S_{xy}\tilde{M}^z_\beta S_{xy}\right]R^y_{\pi/2}\left[S_{xy}\tilde{M}^z_\alpha S_{xy}\right] \\ &= S_{xy}R^y_{\pi/2}\tilde{M}^z_\beta R^y_{-\pi/2}S_{xy}S_{xy}\tilde{M}^z_\alpha S_{xy} \\ &= S_{xy}R^y_{\pi/2}\tilde{M}^z_\beta R^y_{-\pi/2}\tilde{M}^z_\alpha S_{xy} \\ &= S_{xy}R^y_{\pi/2}\left[S_{yz}\left(\tilde{M}^z_\beta\right)^{-1}S_{yz}\right]R^y_{-\pi/2}\tilde{M}^z_\alpha S_{xy} \\ &= S_{xy}R^y_{-\pi/2}S_{xy}\left(\tilde{M}^z_\beta\right)^{-1}S_{xy}R^y_{\pi/2}\tilde{M}^z_\alpha S_{xy} \\ &= S_{xy}R^y_{-\pi/2}\left(\tilde{M}^z_\beta\right)^{-1}R^y_{\pi/2}\tilde{M}^z_\alpha S_{xy} \\ &= S_{xy}M_{\alpha,-\beta}S_{xy}, \end{aligned} \tag{A6}$$

which means that changing θ_x from β to $-\beta$ results in a reflection of Lagrangian topology through the xy plane. Therefore, the cases $\theta_x = \beta$ and $\theta_x = \pi - \beta$ are the same up to symmetry, and it is only necessary to consider $0 \leqslant \theta_x \leqslant \pi/2$.

Changing θ_z from α to $-\alpha$ results in a similar symmetry using both (A3) and (A6):

$$\begin{aligned} M_{\alpha,\beta} &= S_1 M^{-1}_{\beta,\alpha}S_1 \quad \text{by(A3)} \\ &= S_1(S_{xy}M_{\beta,-\alpha}S_{xy})^{-1}S_1 \quad \text{by(A6)} \\ &= S_1 S_{xy}M^{-1}_{\beta,-\alpha}S_{xy}S_1 \\ &= S_1 S_{xy}(S_1 M_{-\alpha,\beta}S_1)S_{xy}S_1 \quad \text{by(A3)} \\ &= S_{yz}M_{-\alpha,\beta}S_{yz}. \end{aligned} \tag{A7}$$

Therefore, changing θ_z from α to $-\alpha$ results in a reflection of Lagrangian topology through the yz plane, and it is only necessary to consider $0 \leqslant \theta_z \leqslant \pi/2$.

Furthermore, the symmetries (A1) and (A2) also apply to the continuum model of the granular BST flow studied in [7,21,33], and hence the symmetries (A3)–(A7) also apply. These symmetries can also be readily adapted to more general rotation protocols such as nonorthogonal rotation axes and multiple (i.e., more than two) rotation axes.

APPENDIX B: CONJUGATE ITINERARIES

As a result of a special property of the BST PWI, chains of cells with at least one cell in the atom P_4 have a conjugate with equal period and size. This means that finding one cell not only gives information about all the cells in its chain, but also the cells in its conjugate chain. Cell conjugacy derives from the following relations:

$$\begin{aligned} \left(R_1^{(-\alpha,-\beta)}\right)^{-1} &= R^z_\alpha R^x_\beta \\ &= R^x_{-\beta}R^x_\beta R^z_\alpha R^x_\beta \\ &= R^x_{-\beta}R_1^{(\alpha,\beta)}R^x_\beta, \end{aligned} \tag{B1}$$

$$\begin{aligned} \left(R_2^{(-\alpha,-\beta)}\right)^{-1} &= R^z_{\alpha+\pi}R^x_\beta \\ &= R^x_{-\beta}R^x_\beta R^z_{\alpha+\pi}R^x_\beta \\ &= R^x_{-\beta}R_2^{(\alpha,\beta)}R^x_\beta, \end{aligned} \tag{B2}$$

$$\begin{aligned} \left(R_{41}^{(-\alpha,-\beta)}\right)^{-1} &= R^z_{\alpha+\pi}R^x_{\beta+\pi}R^z_\alpha R^x_\beta \\ &= R^x_{-\beta}\left(R^x_\beta R^z_{\alpha+\pi}R^x_{\beta+\pi}R^z_\alpha\right)R^x_\beta \\ &= R^x_{-\beta}R_{32}^{(\alpha,\beta)}R^x_\beta, \end{aligned} \tag{B3}$$

where $R_{1-4}^{(\alpha,\beta)}$ are the rotations produced by the BST PWI in each of the atoms with $(\theta_z,\theta_x) = (\alpha,\beta)$; and $R_{41} = R_1R_4$ and $R_{32} = R_2R_3$ are the net rotations produced by the 41 and 32 itineraries, respectively. Therefore, for any itinerary of the form $w41$ where $w = w_0w_1\ldots w_M$ is a word consisting of 1's

and 2's, it follows that

$$\begin{aligned}\left(R_{w41}^{(-\alpha,-\beta)}\right)^{-1} &= \left(R_{41}^{(-\alpha,-\beta)}\right)^{-1}\left(R_{w}^{(-\alpha,-\beta)}\right)^{-1}\\ &= \left(R_{41}^{(-\alpha,-\beta)}\right)^{-1}\prod_{i=0}^{M}\left(R_{w_{M-i}}^{(-\alpha,-\beta)}\right)^{-1}\\ &= R_{-\beta}^{x}R_{32}^{(\alpha,\beta)}R_{\beta}^{x}\prod_{i=0}^{M}R_{-\beta}^{x}R_{w_{M-i}}^{(\alpha,\beta)}R_{\beta}^{x}\\ &= R_{-\beta}^{x}R_{32\mathrm{rev}(w)}^{(\alpha,\beta)}R_{\beta}^{x}, \end{aligned} \tag{B4}$$

where $\mathrm{rev}(w) = w_M w_{M-1}\ldots w_0$ is the reverse of w. Since each of $R_{1-4}^{(\alpha,\beta)}$ is an instance of the BST PWI $M_{\alpha,\beta}$, from Eqs. (A6) and (A7) it follows that

$$\begin{aligned}\left(R_{w41}^{(\alpha,\beta)}\right)^{-1} &= R_{\beta}^{x}R_{32\mathrm{rev}(w)}^{(-\alpha,-\beta)}R_{-\beta}^{x}\\ &= R_{\beta}^{x}S_{xy}S_{yz}R_{32\mathrm{rev}(w)}^{(\alpha,\beta)}S_{yz}S_{xy}R_{-\beta}^{x}\\ &= R_{\beta}^{x}R_{\pi}^{y}R_{32\mathrm{rev}(w)}^{(\alpha,\beta)}R_{\pi}^{y}R_{-\beta}^{x}. \end{aligned} \tag{B5}$$

This means that if $\boldsymbol{x}$ is the center of the cell with itinerary $w41$, i.e., $R_{w41}^{(\alpha,\beta)}(\boldsymbol{x}) = \boldsymbol{x}$, then $R_{\beta}^{x}R_{\pi}^{y}R_{32\mathrm{rev}(w)}^{(\alpha,\beta)}R_{\pi}^{y}R_{-\beta}^{x}(\boldsymbol{x}) = \boldsymbol{x}$, and hence

$$R_{32\mathrm{rev}(w)}^{(\alpha,\beta)}\left[R_{\pi}^{y}R_{-\beta}^{x}(\boldsymbol{x})\right] = R_{\pi}^{y}R_{-\beta}^{x}(\boldsymbol{x}). \tag{B6}$$

Therefore, $\boldsymbol{z} = R_{\pi}^{y}R_{-\beta}^{x}(\boldsymbol{x})$ is the center of the cell with itinerary $32\mathrm{rev}(w)$, assuming it is in the atom P_3, and its chain of cells is referred to as the *conjugate* cells. Furthermore, the cell in P_4 with itinerary $41w$ is in the same group of cells as $\boldsymbol{x}$, with center $\boldsymbol{y}$ satisfying $R_{41}(\boldsymbol{y}) = \boldsymbol{x}$, so

$$\boldsymbol{z} = R_{\pi}^{y}R_{-\beta}^{x}R_{41}(\boldsymbol{x}) = R_{\beta}^{\boldsymbol{u}}(\boldsymbol{x}), \tag{B7}$$

where $\boldsymbol{u} = R_{\alpha}^{z}(-1,0,0)$ is the point where the cutting lines $\mathcal{D}_{1-3}$ meet. Since $R_{\beta}^{\boldsymbol{u}}P_4$ is contained in P_3, demonstrated by the red region inside P_3 (blue) in Fig. 12, this guarantees that $\boldsymbol{z}$ is in P_3, and so the conjugate cells always exist. Figure 12 suggests that every cell in P_4 has a conjugate in P_3, meaning the cell structure in P_3 captures that of P_4. Particles must repeatedly visit either P_3 or P_4 throughout their itinerary, otherwise the x coordinate would approach infinity, it therefore follows that every chain of cells has at least one cell in either P_3 or P_4. Combining this with conjugacy, the complete set of cell types (size and shape) can be found entirely in P_3.

Furthermore, the reflection-reversal symmetry (A5) imposes additional constraint when $\theta_z = \theta_x$. The image $M_{\alpha,\beta}R_{\beta}^{\boldsymbol{u}}P_4$ of the conjugate cells under the BST PWI [the red points in P_2 (green) in Fig. 12] is contained in P_2, and must be symmetric about the line $z = -x$. Hence, the cells in P_4 and their conjugates in P_3 must also be symmetric, with symmetry lines shown in each atom in Fig. 12. This means that the cells that only occur once in P_4, like those with itineraries $\mathcal{I}(m,q)$, must have their center on the symmetry line. Hence, the center is equidistant to the cutting line $\mathcal{D}_2$ (green) and the domain boundary ∂S, which is reflected in Fig. 9 by the equidistance curves that coincide with $\theta_x = \theta_z$. This constraint on Lagrangian topology leads to the generally lower mixing efficacy along the line $\theta_z = \theta_x$.

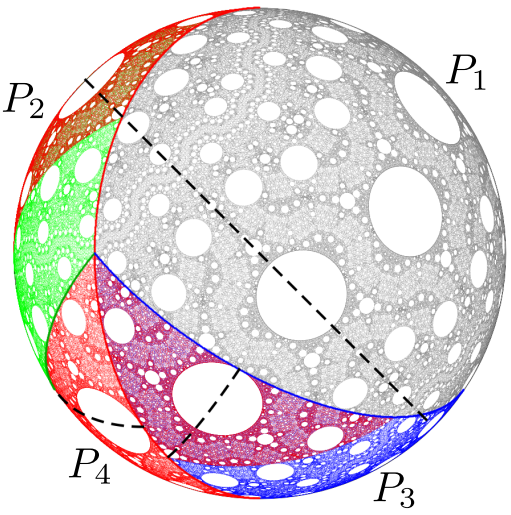

FIG. 12. The exceptional set for the BST PWI with $\theta_z = \theta_x = 4\pi/15$. Points in P_1–P_4 are colored gray, green, blue, and red, respectively. The image of P_4 under the rotation $R_{\theta_x}^{\boldsymbol{u}}$, where $\boldsymbol{u} = R_{\theta_z}^{z}(-1,0,0)$, is shown as the red points in P_3 (blue), illustrating the conjugacy between P_4 and P_3. The image of P_4 under $M_{\theta_z,\theta_x}R_{\theta_x}^{\boldsymbol{u}}$ is shown as the red points contained in P_2 (green). The black dashed symmetry line $z = -x$ corresponding to the reflection-reversal symmetry (A5) yields symmetries in the P_3 and P_4 atoms also.

APPENDIX C: WRAPPING MULTIPLICITY

To understand why resonances occur on and near the lines of constant ratio $\theta_x/\theta_z = \tan\beta$ for $\beta = \pi/(2m)$, $m = 2,3,\ldots$, we consider the limit as $\theta_z,\theta_x \to 0$, keeping their ratio fixed, e.g., the limit towards the origin along one of the dashed lines in Fig. 5. By considering this limit, the fundamental nature of particle trajectories at small positive values of θ_z,θ_x can be understood since they shadow trajectories in the limit. For instance, the wrapping multiplicity of particles in the limit can be used to predict the wrapping multiplicity slightly away from the limit. Furthermore, properties such as wrapping multiplicity are shared even at larger values of θ_z,θ_x.

By assigning a fixed arbitrary rotation rate ω to the z- and x-axis rotation phases, the BST PWI can be written as the integral

$$M_{\theta_z,\theta_x}(\boldsymbol{x}) = \int_0^{T_z+T_x} \boldsymbol{V}(\boldsymbol{x},t)dt, \tag{C1}$$

where

$$\boldsymbol{V}(\boldsymbol{x},t) = \begin{cases}\boldsymbol{V}^{z}(\boldsymbol{x}), & \text{for} \quad 0 \leqslant t \leqslant T_z\\ \boldsymbol{V}^{x}(\boldsymbol{x}), & \text{for} \quad T_z < t \leqslant T_z + T_x\end{cases} \tag{C2}$$

and $\boldsymbol{V}^{z}$, $\boldsymbol{V}^{x}$ are velocity fields corresponding to z- and x-axis rotations at a constant rate ω, and $T_z = \theta_z/\omega$, $T_x = \theta_x/\omega$. Periodic boundary conditions are enforced during the integration of Eq. (C1), such that if a particle reaches the domain boundary ∂S, it is reflected across the plane spanned by the y axis and the current rotation axis. For example, if a particle reaches ∂S during the z-axis rotation, $0 \leqslant t \leqslant T_z$, then it is reflected across the yz plane. This is representative of a half-full spherical granular tumbler flow in the limit of an infinitely thin flowing layer [7]. Therefore, the limit as

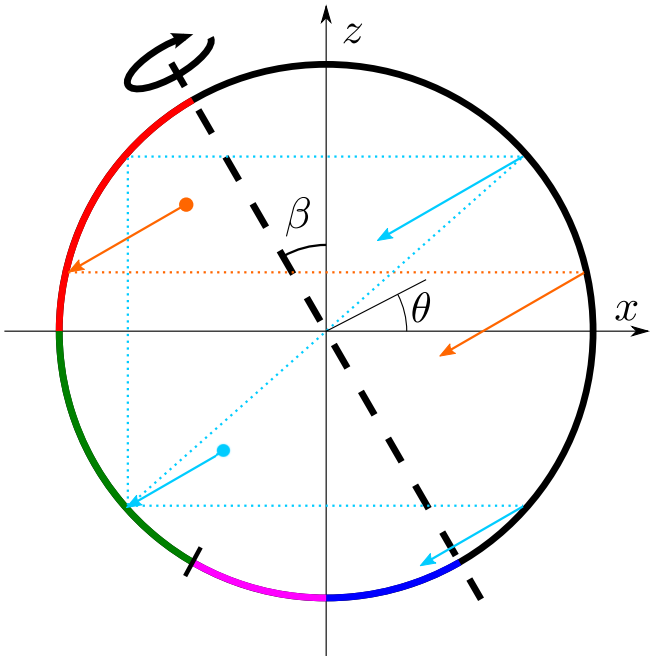

FIG. 13. The BST PWI in the limit as $\theta_z,\theta_x \to 0$ with constant ratio $\theta_x/\theta_z = \tan\beta$. The rotation axis $z = \tan(\pi/2+\beta)x$ is indicated by the dashed black line. The segments of ∂S where particles experience the different periodic boundary conditions described in Eq. (C4) are colored red, green, purple, and blue, respectively. Example particle trajectories that meet the red and green segments of ∂S are shown in orange and light blue, starting from the points marked with circles. Note that when the light blue point meets the green segment of ∂S, it has two images due to the multivalued periodic boundary conditions.

$\theta_z,\theta_x \to 0$ with $\theta_x/\theta_z = \tan\beta$ is equivalent to the limit as $T_z,T_x \to 0$ with $T_x/T_z = \tan\beta$, which is the limit of infinitely fast switching between the z- and x-axis rotation velocity fields. Therefore, in the limit $\theta_z,\theta_x \to 0$ particles are governed by the velocity field $\boldsymbol{V}_{\text{ave}}$, given by the weighted average of the velocity fields in each rotation phase, i.e.,

$$\boldsymbol{V}_{\text{ave}} = \frac{T_z\boldsymbol{V}^z + T_x\boldsymbol{V}^x}{T_z+T_x}, \tag{C3}$$

which is equal to the velocity field corresponding to rotation about the single axis $(-\sin\beta,0,\cos\beta)$, shown as the dashed black line in Fig. 13, with rotation rate ω.

While particle trajectories in the limit $\theta_z,\theta_x \to 0$ are simple in the interior of the domain, the periodic boundary conditions, inherited from the atoms P_{2-4}, introduce complexity. At positive values of θ_z,θ_x, particles only experience the periodic boundary conditions in the atoms P_{2-4}, when they cross the infinitely thin flowing layer during the z-axis rotation (P_2), the x-axis rotation (P_3), or both (P_4). In the limit $\theta_z,\theta_x \to 0$, it is natural that particles should experience the same reflections when they reach ∂S, yielding periodic boundary conditions. However, it is not always clear which atom's boundary conditions should be used because multiple atoms collapse onto some segments of ∂S in the limit $\theta_z,\theta_x \to 0$. Letting $\theta = \arg(x+iz)$ be the polar angle on ∂S, only the atom P_2 collapses onto the segment $\pi/2+\beta \leqslant \theta \leqslant \pi$ (red) in Fig. 13, and so all particles that meet this segment of ∂S experience the same periodic boundary conditions as those in P_2 for positive values of θ_z,θ_x, i.e., they are reflected across the yz plane. This is demonstrated by the trajectory of the orange particle. Similarly, only the atom P_3 collapses onto the segment $3\pi/2 < \theta \leqslant 3\pi/2+\beta$ (dark blue) in Fig. 13, so particles that meet this segment of ∂S experience the same periodic boundary conditions as P_3 for positive θ_z,θ_x, i.e., they are reflected across the xy plane. The atoms P_{2-4} all collapse onto the segment $\pi < \theta \leqslant 3\pi/2-\beta$ (green) in Fig. 13, so it is unclear which periodic boundary condition should be used. For positive values of θ_z,θ_x, particles in P_2 are reflected through the yz plane when they meet ∂S, like in the red segment; particles in P_3 are reflected through the xy plane when they meet ∂S, like the dark blue segment; and particles in P_4 are reflected through the yz plane during the z-axis rotation, then reflected through the xy plane during the x-axis rotation, a net reflection through the origin if they occur sequentially. These three possibilities lead to two possible periodic boundary conditions for the green segment of ∂S in the limit $\theta_z,\theta_x \to 0$, demonstrated by the light blue particle trajectory in Fig. 13, where it is noted that since the xy reflection is on the red segment, it is also reflected across the yz plane. Similarly, the atoms P_{2-4} all collapse onto the segment $3\pi/2-\beta < \theta \leqslant 3\pi/2$ (magenta) in Fig. 13, again yielding multivalued periodic boundary conditions: reflection through the xy plane and reflection through the origin. These periodic boundary conditions can be summarized as follows:

$$F(\theta) = \begin{cases} -\theta+\pi, & \text{for} \quad \pi/2+\beta \leqslant \theta \leqslant \pi \\ (-\theta+\pi,\theta+\pi), & \text{for} \quad \pi < \theta \leqslant 3\pi/2-\beta \\ (-\theta,\theta+\pi), & \text{for} \quad 3\pi/2-\beta < \theta \leqslant 3\pi/2 \\ -\theta, & \text{for} \quad 3\pi/2 < \theta \leqslant 3\pi/2+\beta. \end{cases} \tag{C4}$$

Starting from a position $-\pi/2+\beta < \theta < \pi/2+\beta$ on the black segment of ∂S, denoted ∂S_1, the rotational flow takes the particle to the point $G(\theta) = -\theta-\pi+2\beta$ on the opposite (colored) boundary segment, denoted ∂S_2, i.e., the reflection across the plane $z = \tan(\beta-\pi/2)x$ (the black dashed line in Fig. 13). Therefore, the map from ∂S_2 to itself is given by

$$G[F(\theta)] = \begin{cases} \theta+2\beta, & \frac{\pi}{2}+\beta \leqslant \theta \leqslant \pi \\ (\theta+2\beta,-\theta+2\beta), & \pi < \theta \leqslant \frac{3\pi}{2}-\beta \\ (\theta-\pi+2\beta,-\theta+2\beta), & \frac{3\pi}{2}-\beta < \theta \leqslant \frac{3\pi}{2} \\ \theta-\pi+2\beta, & \frac{3\pi}{2} < \theta \leqslant \frac{3\pi}{2}+\beta. \end{cases} \tag{C5}$$

In every case, the map is $\pm\theta+2\beta \bmod \pi$, hence, the set of all iterates of θ is contained in $\partial S_2 \cap \{\pm\theta+2k\beta, k \in \mathbb{Z}\}$. Considering particle trajectories where only horizontal reflections through the yz plane are taken into account in the green segment, and only vertical reflections through the xy plane are taken into account in the purple segment, the map is given by

$$G[F(\theta)] = \begin{cases} \theta+2\beta, & \frac{\pi}{2}+\beta \leqslant \theta \leqslant \frac{3\pi}{2}-\beta \\ \theta-\pi+2\beta, & \frac{3\pi}{2}-\beta < \theta \leqslant \frac{3\pi}{2}+\beta. \end{cases} \tag{C6}$$

Therefore, every point in $\partial S_2 \cap \{\theta+2k\beta, k \in \mathbb{Z}\}$ can be found as an iterate of θ. Likewise, considering one diagonal

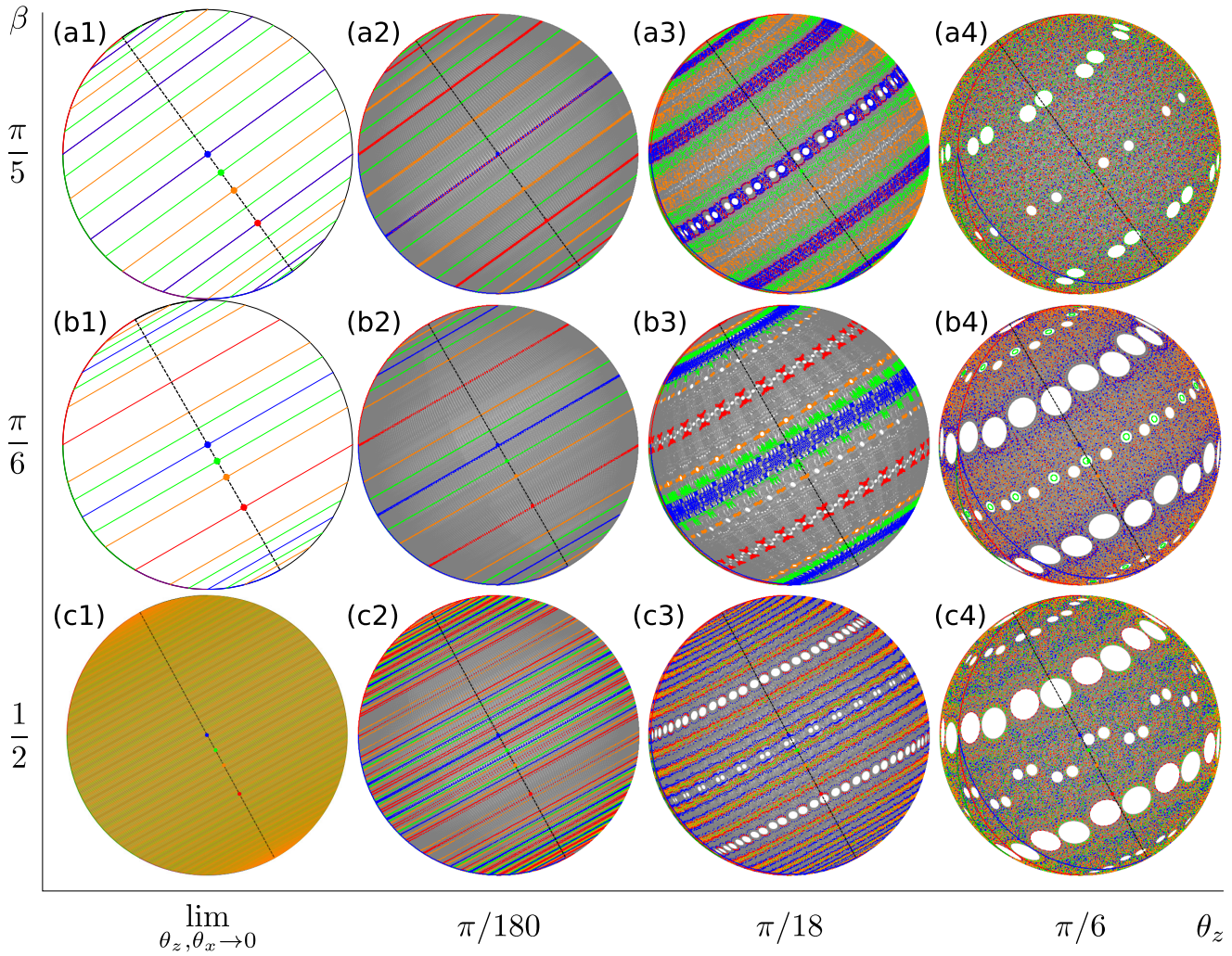

FIG. 14. Particle trajectories in the limit as $\theta_z,\theta_x \to 0$ and at small values of θ_z,θ_x, for constant ratios $\theta_x/\theta_z = \tan\beta$. The first column shows the trajectories of four particles with streamlines that meet the boundary at $\theta = \beta, 3\beta/4, \beta/2, 0$ colored blue, green, orange, and red, respectively. In the other columns, the same particles are tracked for θ_z as shown and $\theta_x = \tan(\beta)\theta_z$, combined with the exceptional set shown in gray.

periodic boundary crossing, $\theta \mapsto -\theta + 2\beta$, in the green or purple segments, followed by all horizontal and vertical crossings [Eq. (C6)], it follows that $\partial S_2 \cap \{-\theta + 2k\beta, k \in \mathbb{Z}\}$ is also contained in the set of all iterates of θ. We have therefore shown that the set of all iterates of θ under $G \circ F$ is equal to $\partial S_2 \cap \{\pm\theta + 2k\beta, k \in \mathbb{Z}\}$. Hence, when β/π is rational, the set of all iterates of θ is finite, and particle trajectories throughout the domain are periodic, demonstrated by Figs. 14(a1) and 14(b1). Conversely, when β/π is irrational, the set of all iterates is infinite, densely filling ∂S_2, meaning particle trajectories never return to their initial position, and densely fill the entire HS, as demonstrated by Fig. 14(c1).

The rational cases are worthy of consideration in more detail. When $\beta = m\pi/n$ and n is odd, the set of boundary images $\partial S_2 \cap \{\pm\theta + 2k\beta, k \in \mathbb{Z}\}$ generally has $2n$ elements, indicating that particles wrap around the HS $2n$ times before returning to their initial position [demonstrated by the green trajectory in Fig. 14(a1)]. However, when $\theta = j\beta$ or $j\beta/2$, the set of boundary images has n elements, as $\theta \equiv -\theta \mod 2\beta$ [the blue and orange trajectories in Fig. 14(a1)]. Similarly, when $\beta = m\pi/n$ and n is even, the set of boundary images generally has n elements [as the denominator of 2β is $n/2$, demonstrated by the green and orange trajectories in Fig. 14(b1)], and, when $\theta = j\beta$, the set of boundary images has $n/2$ elements [the red and blue trajectories in Fig. 14(b1)].

At small values of θ_z,θ_x, particles shadow the trajectories in the limit, demonstrated by Fig. 14. Therefore, the number of times particles wrap around the HS is determined by the wrapping multiplicity of nearby trajectories in the limit, which is equal to the size of the set of boundary images $\partial S_2 \cap \{\pm\theta + 2k\beta, k \in \mathbb{Z}\}$. The angle β therefore has a significant impact on the possible wrapping multiplicities, and hence the size of cells and resonances. Cells with a high wrapping multiplicity must pass through the atoms P_{1-4} in the "skinny" sections, and hence are generally smaller than those with lower wrapping multiplicity that occupy the "fat" sections of P_{1-4}. Therefore, the lowest wrapping multiplicities, corresponding to protocols of the form $\theta_x/\theta_z = \tan(m\pi/n)$ with n even, give rise to the largest cells. Note that further from the limit, cells are robust under perturbation in β, explaining why period-11 cells

with the same itinerary exist for $\theta_z = \pi/6$ with $\beta = \pi/6$ and $\beta = 1/2 \approx \pi/6.28$ [Figs. 14(b4) and 14(c4)]. These period-11 cells have wrapping multiplicity equal to 2, which derives from the trajectory of the red particle in Fig. 14(b1).

APPENDIX D: TONGUE OVERLAP

In this Appendix, we uncover the reason for the coincidence of two of the annihilation boundaries, corresponding to $\mathcal{D}_{1,2}$, and the equidistance curve

$$d(\boldsymbol{x},\mathcal{D}_1) = d(\boldsymbol{x},\mathcal{D}_2) \tag{D1}$$

for itineraries of the form $\mathcal{I}(m,q) = 41^{q-1}(21^{q-1})^{m-1}$, with q fixed and $m = 1,2,\ldots$. We show that the cells' centers all lie on a great circle $\mathcal{C}^*$ that passes through the point $\boldsymbol{u} = R^z_{\theta_z}(-1,0,0)$ where the three cutting lines meet, as demonstrated in Fig. 15. Hence, all the cells annihilate when $\mathcal{C}^*$ coincides with $\mathcal{D}_1$ or $\mathcal{D}_2$, and all the cells are equidistant to $\mathcal{D}_{1,2}$ when $\mathcal{C}^*$ bisects $\mathcal{D}_{1,2}$.

Letting $\mathcal{R}_1$ denote the net rotation associated with the itinerary $\mathcal{I}(1,q) = 41^{q-1}$ and $\mathcal{R}_2$ denote the net rotation associated with the itinerary 21^{q-1}, it follows that the net rotation for the itinerary $\mathcal{I}(m,q)$ is $\mathcal{R}(m,q) = \mathcal{R}_2^{m-1}\mathcal{R}_1$. The rotation $\mathcal{R}_2$ can be represented via its angle and axis $(\theta,\boldsymbol{v})$ or, equivalently, as the quaternion

$$\{q_1,q_2,q_3,q_4\} = \{\cos(\theta/2), \sin(\theta/2)\boldsymbol{v}\}. \tag{D2}$$

Hence, the rotation $\mathcal{R}_2^m$ has angle-axis form $(m\theta,\boldsymbol{v})$ and quaternion form

$$\mathcal{R}_2^m = \{\cos(m\theta/2), \sin(m\theta/2)\boldsymbol{v}\}. \tag{D3}$$

Therefore, the net rotation $\mathcal{R}(m+1,q)$ has quaternion representation

$$\begin{aligned}\mathcal{R}(m+1,q) &= \mathcal{R}_2^m\mathcal{R}_1 \\ &= \{\cos(m\theta/2), \sin(m\theta/2)\boldsymbol{v}\}\mathcal{R}_1 \\ &= [\cos(m\theta/2)I + \sin(m\theta/2)\{0,\boldsymbol{v}\}]\mathcal{R}_1 \\ &= \cos(m\theta/2)\mathcal{R}_1 + \sin(m\theta/2)\{0,\boldsymbol{v}\}\mathcal{R}_1 \\ &= \cos(m\theta/2)\boldsymbol{A} + \sin(m\theta/2)\boldsymbol{B},\end{aligned} \tag{D4}$$

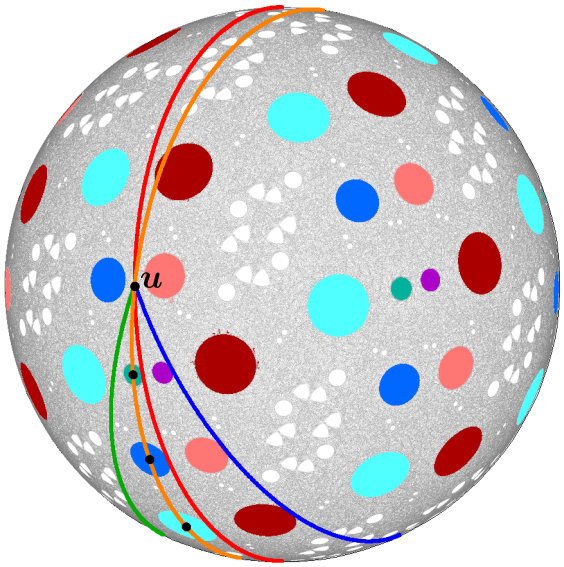

FIG. 15. The exceptional set (gray) for the BST PWI with $(\theta_z,\theta_x) = (1.012,0.3796)$. The cells with base itineraries 41^2, 41^221^2, $41^2(21^2)^2$ and their conjugates are colored. The great circle $\mathcal{C}^*$ that passes through the centers of all the cells in P_4 and the point $\boldsymbol{u}$ where $\mathcal{D}_{1-3}$ meet is shown in orange.

where I is the identity quaternion and $\boldsymbol{A} = \mathcal{R}_1$, $\boldsymbol{B} = \{0,\boldsymbol{v}\}\mathcal{R}_1$ are quaternions that are independent of m. This means the (non-normalized) axes of rotation corresponding to the itineraries $\mathcal{I}(m,q)$ for $m = 1,2,\ldots$, given by the vector parts [34] of the quaternions $\mathcal{R}(m,q)$, are all linear combinations of the vector parts $\boldsymbol{a} = \boldsymbol{A}[2,3,4]$ and $\boldsymbol{b} = \boldsymbol{B}[2,3,4]$. Hence, the centers of the corresponding cells are all coplanar, lying in the plane spanned by $\boldsymbol{a}$ and $\boldsymbol{b}$, and therefore all lie on the same great circle $\mathcal{C}^*$.

It remains to show that $\mathcal{C}^*$ passes through the point $\boldsymbol{u}$ where $\mathcal{D}_{1-3}$ meet. By directly computing the expressions for $\boldsymbol{u}$, $\boldsymbol{a}$, and $\boldsymbol{b}$, it can be shown that $\boldsymbol{u}\cdot(\boldsymbol{a}\times\boldsymbol{b}) = 0$, and hence $\boldsymbol{u}$, $\boldsymbol{a}$ and $\boldsymbol{b}$ are all coplanar, as desired.

[1] S. Wiggins and J. M. Ottino, Philos. Trans. R. Soc. London A **362**, 937 (2004).
[2] D. V. Khakhar, H. Rising, and J. M. Ottino, J. Fluid Mech. **172**, 419 (1986).
[3] J. M. Ottino, *The Kinematics of Mixing: Stretching, Chaos, and Transport* (Cambridge University Press, Cambridge, 1989).
[4] M. Lemieux, F. Bertrand, J. Chaouki, and P. Gosselin, Chem. Eng. Sci. **62**, 1783 (2007).
[5] J. Doucet, F. Bertrand, and J. Chaouki, Granular Matter **10**, 133 (2008).
[6] E. Alizadeh, H. Hajhashemi, F. Bertrand, and J. Chaouki, Chem. Eng. Sci. **97**, 354 (2013).
[7] R. Sturman, S. W. Meier, J. M. Ottino, and S. Wiggins, J. Fluid Mech. **602**, 129 (2008).
[8] Z. Zaman, M. Yu, P. P. Park, J. M. Ottino, R. M. Lueptow, and P. B. Umbanhowar, arXiv:1706.00864.
[9] M. Keane, Math. Z. **141**, 25 (1975).
[10] A. Goetz, Discrete Continu. Dynam. Syst. **4**, 593 (1998).
[11] A. Goetz, *Piecewise Isometries: An Emerging Area of Dynamical Systems* (Birkhäuser, Basel, 2003).
[12] L. O. Chua and T. Lin, IEEE Circuits Syst. **35**, 648 (1988).
[13] P. Ashwin, Phys. Lett. A **232**, 409 (1997).
[14] A. Scott, C. Holmes, and G. Milburn, Phys. D (Amsterdam) **155**, 34 (2001).
[15] A. Scott, Phys. D (Amsterdam) **181**, 45 (2003).
[16] S. W. Jones and H. Aref, Phys. Fluids **31**, 469 (1988).
[17] L. D. Smith, M. Rudman, D. R. Lester, and G. Metcalfe, Chaos **26**, 023113 (2016).
[18] P. P. Park, P. B. Umbanhowar, J. M. Ottino, and R. M. Lueptow, Chaos **26**, 073115 (2016).
[19] P. P. Park, T. F. Lynn, P. B. Umbanhowar, J. M. Ottino, and R. M. Lueptow, Phys. Rev. E **95**, 042208 (2017).
[20] G. Juarez, I. C. Christov, J. M. Ottino, and R. M. Lueptow, Chem. Eng. Sci. **73**, 195 (2012).

[21] R. Sturman, Adv. Appl. Mech. **45**, 51 (2012).
[22] G. Juarez, R. M. Lueptow, J. M. Ottino, R. Sturman, and S. Wiggins, Europhys. Lett. **91**, 20003 (2010).
[23] The map can be extended to a PWI over the entire sphere by performing the same operations in the y^+ hemisphere, and this would not change the properties of the PWI.
[24] We use the same criterion outlined in [19] to determine how many iterations are sufficient.
[25] Note that the parameter range $0 \leqslant \theta_z, \theta_x \leqslant \pi/2$ captures the entire protocol space due to the symmetries (A6) and (A7) described in Appendix A.
[26] J. G. Franjione, C. Leong, and J. M. Ottino, Phys. Fluids A **1**, 1772 (1989).
[27] J. G. Franjione and J. M. Ottino, Philos. Trans. R. Soc. London A **338**, 301 (1992).
[28] J. M. Ottino, F. J. Muzzio, M. Tjahjadi, J. G. Franjione, S. C. Jana, and H. A. Kusch, Science **257**, 754 (1992).
[29] D. R. Lester, G. Metcalfe, M. G. Trefry, A. Ord, B. Hobbs, and M. Rudman, Phys. Rev. E **80**, 036208 (2009).
[30] O. S. Galaktionov, P. D. Anderson, and G. W. M. Peters, Phys. Fluids **12**, 469 (2000).
[31] Z. Pouransari, M. F. M. Speetjens, and H. J. H. Clercx, J. Fluid Mech. **654**, 5 (2010).
[32] L. D. Smith, M. Rudman, D. R. Lester, and G. Metcalfe, Chaos **26**, 053106 (2016).
[33] I. C. Christov, R. M. Lueptow, J. M. Ottino, and R. Sturman, SIAM J. Appl. Dyn. Syst. **13**, 901 (2014).
[34] For a quaternion $\{a,b,c,d\}$, a is termed the *scalar* part and (b,c,d) is termed the *vector* part.